Does the Sun have a dark disk?

Gustavo F. S. Alves,[1,2] Susan Gardner,[3,*] Pedro Machado,[1] and Mohammadreza Zakeri[3]

[1]*Fermi National Accelerator Laboratory, Batavia, Illinois 60510, USA*

[2]*Departamento de Física Matemática, Instituto de Física Universidade de São Paulo, 05315-970 São Paulo, Brazil*

[3]*Department of Physics and Astronomy, University of Kentucky, Lexington, Kentucky 40506-0055, USA*

(Received 12 June 2024; revised 31 March 2025; accepted 7 April 2025; published 30 April 2025)

The Sun is not quite a perfect sphere, and its oblateness, thought to be induced through its rotation, has been measured using optical observations of its radius. Its gravitational quadrupole moment can then be deduced using solar models, or through helioseismology, and it can also be determined from measurements of its gravitational effects on Mercury's orbit. The various assessments do not appear to agree, with the most complete and precise orbital assessments being in slight excess of other determinations. This may speak to the existence of a nonluminous disk or ring, where we also note evidence for a circumsolar dust ring within Mercury's orbit from the Solar TErrestrial RElations Observatory (STEREO) mission. Historically, too, a protoplanetary disk may have been key to reconciling the Sun's metallicity with its neutrino yield. The distribution of the nonluminous mass within Mercury's orbit can modify the relative size of the optical and orbital quadrupole moments in different ways. We develop how we can use these findings to limit the mass of a dark disk, ring, or halo in the immediate vicinity of the Sun, and we note how future observational studies of the inner Solar System can not only refine these constraints but can also help to identify and to assess the mass of its dark-matter component.

DOI: 10.1103/PhysRevD.111.083057

I. INTRODUCTION

As first noted by Dicke in 1964, an optical measurement of the solar oblateness of sufficient size could contribute significantly to Mercury's perihelion precession and thus test Einstein's theory of general relativity (GR) [1,2]. A subsequent measurement of the oblateness $\Delta_\odot$, defined as the difference in the equatorial and polar radii over the mean solar radius, gave $(5.0 \pm 0.7) \times 10^{-5}$, apparently challenging GR at the sub-10% level [3]. In the intervening decades, the ability to assess the oblateness has shown steady and significant progress, and space-based studies have also been made, yielding refined errors. Moreover, the impact of magnetic-field-correlated brightness variations on optical measurements of the oblateness have been noted and quantified [4], removing disagreements and mitigating earlier puzzles [3,5,6]. Ultimately, with improved measurements and theory, the gravitational quadrupole moment J_2 of the Sun can be determined, with a nonzero value of about 2×10^{-7}, and refined determinations of its value from improved measurements of Mercury's orbit also support its approximate value, with the determined errors being some 100–1000 times smaller than that, as we detail. These new levels of sensitivity open a new frontier, in that once negligible effects, such as a circumsolar mass, can become appreciable. Here, we compare the visual and gravitational assessments of J_2 to constrain the mass and distribution of nonluminous matter in the immediate vicinity of the Sun.

Different lines of evidence, from different eras in the Solar System's history, point to the existence of a nonluminous disk. For example, the measured energy spectrum of the solar neutrino flux determines the strength of the CNO cycle in the Sun [7–9] with a rate compatible with high metallicity [10] but not low metallicity [11] solar models. Concomitantly, there is also a long-standing inconsistency between the element abundances determined from the spectroscopy of the surface, as in [11], and those inferred from the interior through helioseismology [11–13]. This solar modeling problem can be mitigated if the interior metallicity of the Sun can differ from that of its surface [14], possibly through the formation of the photosphere with the gas-giant planets in the early Solar System [15]. Later work has shown a metallicity gradient can appear if the Sun formed while within a circumsolar disk [16,17]. Evidence has also been found for a circumsolar dust ring at the approximate location of Mercury's orbit [18]. The excess mass density is estimated at 5%, and the total mass is

*Contact author: susan.gardner@uky.edu

not determined [19]. The origins of such a dust ring are not known, and it could also stem from effects later in the Solar System's history [20]. A nonluminous circumsolar disk could also contain a non-Standard Model, or dark matter, component. The capture of such an exotic component could be considerably enhanced if ordinary matter in a nonluminous disk exists over a significant period in the Solar System's history. We note [21–23] for earlier discussion of the possibility of massive circumsolar rings within Mercury's orbit—and possibly of dark matter [23].

We conclude this section with a sketch of the balance of the paper. The comparison of different assessments of the solar quadrupole moment is key to our ability to probe the matter distribution, and indeed dark matter, in the inner Solar System. Thus, we discuss the various methods in some detail. We first describe how the observed solar oblateness connects to $J_2^{\rm Opt}$, the visible quadrupole moment, before describing how Mercury's measured perihelion precession, along with other data, can be used to determine $J_2^{\rm Orb}$, the quadrupole moment determined through gravitational interactions. Here, we note that, through use of helioseismology, that $J_2^{\rm Heli}$ can also be found, through different methods, though optical measurements of the Sun's surface are also employed. We then discuss possible nonluminous components, including dark matter, and their origin, that could exist within Mercury's orbit. We emphasize that the different possibilities influence the relative sizes of $J_2^{\rm Opt}$, $J_2^{\rm Heli}$, and $J_2^{\rm Orb}$ differently. After considering the world's data on J_2, we describe how the pattern of existing results can limit the mass and distribution of nonluminous matter. Although the existing J_2 results may be impacted by unassessed systematic errors, we find the prospect of physical differences in their assessment to be an intriguing idea worthy of exploration. Finally, we describe future prospects of observational studies of the inner Solar System in making our final summary. In so doing, we offer a perspective on the possible evolution of nonluminous matter constraints, on their possible impact on future, refined GR tests [24], and ultimately on our ability to distinguish conventional nonluminous matter from (exotic) dark matter in the inner Solar System. Although we have emphasized various determinations of the gravitational quadrupole moment, these studies naturally yield limits on solar mass loss, which could also have a dark-matter component, and on odd gravitational moments as well, and we note these and their implications as they arise.

II. OBLATENESS AND THE QUADRUPOLE MOMENT

We first develop how observations of the Sun's surface can be used to determine its oblateness and finally its quadrupole moment. A static, isolated, spherical Sun is perturbed by its rotation. If its center of mass (c.m.) is at rest and centered at the origin of a parametrized post-Newtonian (PPN) coordinate system, its gravitational potential, external to its surface ($r > R_\odot$), becomes [25,26]

$$\phi_{\rm o}(r,\theta) = -\frac{GM_\odot}{r}\left[1 - \sum_{2n}\left(\frac{R_\odot}{r}\right)^{2n} J_{2n} P_{2n}(\cos\theta)\right], \quad (1)$$

where θ is the polar angle from the symmetry axis (colatitude), and the P_{2n} are Legendre polynomials. The solar mass $M_\odot$ is not absolutely known, nor is J_2, the quadrupole-moment parameter, in that from the perspective of Mercury's orbit they are effective quantities that can be modified by mass in the Sun's immediate vicinity. In so noting, we suppose any such excess mass to share its c.m. with that of the Sun. We also note that the apparent azimuthal symmetry of Eq. (1) is not a limitation, because the solar studies we employ are nearly continuous through the Sun's rotational period, making the J_{2n} azimuthally averaged quantities. Moreover, if either external forces act on the Sun's c.m. in an appreciable way or if nonluminous matter within Mercury's orbit shifts the Sun's c.m. from its visible one, then the gravitational potential need no longer be reflection symmetric with respect to its midplane and terms odd in n can appear, via $2n \to n$ in Eq. (1). (We note [27,28] finds a nonzero torque on stars within some 3 kpc of the Sun.) Introducing the effective potential $\Phi = \phi_{\rm o} - \phi_\Omega$ at the surface, where ϕ_Ω is generated by rotation, the oblateness $\Delta_\odot$ can be connected to the gravitational moments via the equipotential condition $\Phi(R_e) = \Phi(R_p)$ to find, working through $n = 4$,

$$\Delta_\odot \equiv \frac{R_e - R_p}{R_\odot} \approx J_1 + \frac{3}{2}J_2 + J_3 + \frac{5}{8}J_4 + \frac{\Omega^2 R_\odot^3}{2GM_\odot}, \quad (2)$$

where R_e, R_p, and $R_\odot$ are the equatorial, polar, and mean solar radius, respectively, and an effective rotation rate Ω emerges under the assumption of axially symmetric differential rotation. We refer to Appendix A for all details. Neglecting all J_i save for J_2 yields the long-known result of [29], whereas setting $J_1 = J_3 = 0$ yields that of [26]. If J_2 is determined from $\Delta_\odot$ with $J_{i\neq 2} = 0$, we term it $J_2^{\rm opt}$.

III. INTERPRETING THE PERIHELION PRECESSION

Some 92% of Mercury's perihelion precession stems from precisely known perturbations from the planets, particularly from Venus, Jupiter, and the Earth/Moon system [30,31]. Effects from non-Newtonian gravitational effects and the Sun's J_2 are also well-known but are more poorly determined [30,31], and their most complete and precise determinations come from analyses [31,32] of near-Mercury radio ranging and Doppler tracking data from the NASA MErcury Surface, Space ENvironment, GEochemistry, and Ranging (MESSENGER) spacecraft

mission [33]. Here, Mercury's mean orbit frame is defined with respect to the International Celestial Reference Frame [34], whose variation in orientation is sufficiently small that its impact on the perihelion determination lies beyond the sensitivity of the MESSENGER data [31]. With this choice, the perihelion precession rate is ultimately determined from the slope of the phase angle determined from fitting the data with a function containing both steadily increasing and periodic time-dependent features. The quantity $\dot{\varpi}$, the rate of perihelion precession along Mercury's orbit plane, appears linearly in time t and contains the gravitoelectric (GE), Einstein-Lense-Thirring (ELT), and solar quadrupole moment contributions within it. In the PPN formalism, the GE effect is linear in β and γ (and is nonzero in GR [35], in which $\beta = \gamma = 1$), with the ELT effect being numerically nearly negligible if the solar angular momentum $S_\odot$ determined from helioseismology is used [36]. Physically, we note β and γ describe the nonlinearity in the superposition law for gravitation and the space curvature produced by a unit rest mass, respectively [25]. In [31], e.g., the ELT effect is absorbed within their error analysis. Nevertheless, a determination of $\dot{\varpi}$ contains β, γ, and J_2, so that additional information is needed to separate them. Using information on γ from the Cassini mission, $\gamma - 1 = (2.1 \pm 2.3) \times 10^{-5}$ [37] and the time structure of the precession angle, both β and J_2 can be determined [31]. The analysis of [31] uses MESSENGER data from its four-year orbital phase (2011–2015), whereas that of [32] uses all of the MESSENGER data over its fly-by and orbital phases (2008–2015). These analyses can employ the Nordtvedt parameter [38,39] constraint $\eta = 4\beta - \gamma - 3 = 0$ of GR as well. The values of J_2 from these studies and others are collected in Tables II, III, IV, and V in Appendix B; we also consider the values that emerge if $\beta = \gamma = 1$, as in GR. These studies also offer constraints on time-dependent effects, particularly through the apparent time independence of the residuals in the perihelion precession fit of [31] and of the estimated rate of change in the solar gravitational parameter $\mu \equiv GM_\odot$. Namely, $\dot{\mu}/\mu = (-6.13 \pm 1.47) \times 10^{-14}$ yr^{-1} [32], to be compared with the planetary ephemerides result of $(-10.2 \pm 1.4) \times 10^{-14}$ yr^{-1} [40], where we note [41] for a review. We return to the implications of these results in Sec. VI.

IV. POSSIBLE NONLUMINOUS COMPONENTS

Although the dust in the Solar System can reflect light [42], it does not emit visible light, and thus, we have classified it as nonluminous matter. A dusty disk appears to exist throughout much of the Solar System [43], and simulations suggest that its structure differentiates between the inner and outer Solar System [44]. A population of micrometeoroids, seeded by collisional grinding of zodiacal dust, may also be relevant within 1 A.U. [45], and still other sorts of nonluminous objects may contribute [46]. We have noted that a ring of dust has been discovered in the path of Mercury's orbit [18], from the STEREO mission [47], and a model of its mass distribution suggests its mass could be about $(1.02\text{–}4.05) \times 10^{12\pm(\approx 1)}$ kg, roughly equivalent to the mass of a single asteroid [20]. Known asteroids range from about 10^{10-21} kg in mass [48].

Yet dust is not the only possibility. Dark matter, e.g., may also contribute. Studies of stellar tracers in the solar neighborhood suggests that the local dark matter density is only some $\rho_{\rm dm} = 0.4$ GeV/cm^3 [49], and a spheroid of that density would contribute a mass of 6×10^{11} kg, or $3 \times 10^{-19} M_\odot$, within Mercury's orbit. Moreover, it has long been thought that gravitational focusing mechanisms exist, modifying the dark-matter velocity distribution and acting to increase the dark matter density within the Solar System [50–56], albeit the total mass added is not very significant. The detailed estimates depend on the dark-matter model and on astrophysical modeling. For example, upon adopting a Weakly Interacting Massive Particle (WIMP) dark-matter candidate within a standard Galactic halo model, the direct detection event rate for gravitationally captured WIMPs on the Solar System has been determined to never exceed 0.1% of the event rate for halo WIMPs [52,57], though gravitational perturbations external to the Solar System could impact the bound WIMP population significantly [57]. More significant variations should be possible in models for which the dark-matter candidate possesses inelastic interactions, as constraints from Liouville's theorem would not apply. Gravitational focusing of unbound dark matter on individual planetary bodies has also been found to yield significant, local density enhancements in their immediate vicinity [51,55] and even ringlike, time-dependent effects [51] that we investigate further.

There have also been studies of the capture of dark matter within celestial bodies, and for models with sufficient dark-matter–matter interactions, significant enhancements over the nominal dark-matter density are possible [58–63], showing that dark matter could contribute nontrivially to the mass of a celestial body within its observed radius. Measurements of the Earth's heat budget do limit, however, the possibility of strong dark-matter–matter interactions [64,65], though some of the internal heating of Jovian planets could speak to planet-bound dark matter [66].

A celestial body can also possess a dark halo, and this can emerge if the dark-matter particle simply possesses self-interactions. In the "gravi-atom" mechanism of [67], for example, two-body scattering, particularly of ultralight dark matter, in the gravitational field of a celestial body can yield dark-matter capture and ultimately a dark halo. We consider this scenario further in Sec. VII. If the dark matter couples to neutrinos, then neutrino oscillation data can probe the Earth's dark halo [68].

The possibility of exotic dark structures, such as exoplanets [69], filaments [70], or other macroscopic objects [71], have also been suggested. These macroscopic objects

need not have a dark matter component, as, say, in the case of magnetic black holes [72], but others, such as primordial black holes (PBHs), can also function as a dark matter candidate and are as yet poorly constrained in the asteroid mass range [73]. Their transits of the Solar System can be limited through planetary ephemerides [74], as well as via observational means [75]. Gravitational wave detection can also probe the possibility of local, macroscopic dark matter [76] and of the Solar System's mass distribution [77]. The Sun and planets can also emit light dark particles, as, e.g., in [78,79]. However, the time rate of change in the gravitational parameter is smaller than that estimated from the net effect of dust capture and the solar wind [32], so that no limit on dark-matter emission is currently possible.

Constraints on all these scenarios emerge from measurements of planetary motion [80–86], which show that the maximum density at the Earth's orbit is limited to be below 10^2–10^5 GeV/cm^3, depending slightly on the profile shape. Somewhat weaker constraints emerge from studies of the inner planets [86]. We emphasize that existing estimates of dark-matter capture on the Solar System, including work within the popular WIMP dark-matter paradigm, fall rather short of these limits [52,53]. There are also constraints on the Earth's own dark halo [66] and on the dark matter density by analyzing the propagation of light in the Solar System [87]. Dark matter would cause time delay and frequency shift of the light, though the constraints are not very stringent [87,88].

In this paper, we develop constraints on the mass and distribution of nonluminous matter external to the Sun and planets and thus of dark-matter models connected to these possibilities. The suggested magnitude of the excess mass we find, were it to come from exotic sources, points preferentially to the possibility of non-WIMP dark-matter candidates, as we detail in Sec. VII.

V. GRAVITATIONAL QUADRUPOLE MOMENT DETERMINATIONS

Determinations of J_2 began decades ago and also range over decades. Three distinct methods have been used. There have been direct optical measurements of the solar oblateness $\Delta_\odot$, which, when combined with theory, as in Eq. (2), yield $J_2^{\rm Opt}$. Helioseismological data probe the structure of the Sun; this, when combined with a model for its structure, can be used to infer $J_2^{\rm Heli}$. Finally, as we have noted, precision measurements of planetary motion can also be used to infer $J_2^{\rm Orb}$. We emphasize that the orbital determinations are sensitive to the existence of mass *within* the orbit in question. In this paper we focus on determinations of $J_2^{\rm Orb}$ from measurements of Mercury's orbit, to address the possibility of nonluminous matter in the immediate region of the Sun. There is a long history of solar oblateness measurements [3,5], with improved assessments once space-based studies became possible [89]. Surface magnetism and other effects can impact the observed shape [90,91], and Fivian *et al.* have provided a corrected assessment that would remove the enhancement from solar magnetism [91]. However, we note that discussions of the shape assessment, and the possibility of a time-dependent solar shape, continues [92–94].

We summarize the most pertinent determinations here and note Appendix B for a more complete list. We report the results for J_n in units of 10^{-7} throughout. From Park *et al.* [31],

$$J_2^{\rm Orb} = 2.25 \pm 0.09; \qquad J_2^{\rm Orb}|_{\beta=\gamma=1} = 2.28 \pm 0.06, \tag{3}$$

whereas from Genova *et al.* [32],

$$J_2^{\rm Orb} = 2.246 \pm 0.022;$$
$$J_2^{\rm Orb}|_{\beta=1;\eta=0} = 2.2709 \pm 0.0044. \tag{4}$$

Here, we quote the quadrupole moment assessment within a PPN framework, as well as its value upon assuming GR. In the first case, Genova *et al.* also find the PPN parameter $\eta = (-6.6 \pm 7.2) \times 10^{-5}$, noting that nonzero η can be associated with a shift in the Solar System barycenter [32] and vice versa. We note appreciable shifts in the central values and smaller uncertainties are associated with the GR limit. Since studies of dark matter always assume that GR is valid, we choose $\beta = \gamma = 1$ ($\eta = 0$) for our studies here. Moreover, the result of Genova *et al.* [32] reflects the use of the full MESSENGER data set, so that we employ the GR limit in Eq. (4) for $J_2^{\rm Orb}$ henceforth.

Before proceeding, however, we pause to consider the gross discrepancy in the errors in the two determinations, as they are significantly different. The origin of this has been investigated by Konopliv *et al.* [95], and it appears that the difference largely stems from a simplifying assumption in the Genova *et al.* [32] analysis, namely, that the Earth's orbit is perfectly known. When the uncertainties in the orbit of the Earth and Mercury generated by all the other planetary bodies are included, then the error in $J_2^{\rm Orb}$ increases by about a factor of 4, explaining the difference in the errors found in the two analyses in the PPN case [95]. Presumably, a similar enlargement appears in the GR case as well, though it would not explain the difference in the errors in the two $J_2^{\rm Orb}$ determinations. In what follows, we employ the GR result of Eq. (4), but are mindful of the expected larger error [95] in considering its significance.

Turning to the optical assessment of $\Delta r \equiv R_e - R_p = (8.01 \pm 0.14)$ milliarcsec (mas) due to Fivian *et al.* [91] using the space-based Reuven Ramaty High Energy Solar Spectroscopic Imager (RHESSI) instrument [96], the value of J_2 can be determined from $J_2 = (2/3)(\Delta r - \Delta r_{\rm surf})/R_\odot$ [5] with $\Delta r_{\rm surf} \approx 7.8$ mas [29] and $R_\odot = 9.5963 \times 10^5$ mas [97], its radius at 1 A.U. [98]. Noting $\Delta r_{\rm surf}/R_\odot$ corresponds to the last term in Eq. (2), they find [91]

$$J_2^{\rm Opt} = 1.46 \pm 1.0, \tag{5}$$

where the error does not include an error in $\Delta r_{\rm surf}$. If we were, rather, to employ the Δr measurement in [92], $\Delta r = 7.20 \pm 0.49$ mas, the associated J_2 would be negative but consistent with zero with a much larger error. For clarity, we reiterate that in this paper we define the *oblateness* as $\Delta_\odot \equiv \Delta r/R_\odot$, which evaluates to $(8.35 \pm 0.15) \times 10^{-6}$, because, in contrast, Fivian *et al.* [91] term Δr the oblateness.

We now turn to the assessments from helioseismology. The $J_2^{\rm Heli}$ comes from observations of the oscillations in the Sun's surface interpreted within a solar model. Here, we highlight the work of Mecheri and Meftah for their use of multiple, space-based solar oscillation data sets and multiple solar evolution models, all within an integral equation approach that eliminates the need for a solar differential rotation model [101]. This is an update of Mecheri *et al.* that uses data from the Michelson Doppler Imager on the Solar and Heliospheric Observatory (SoHO/MDI) and models for the solar differential rotation. Using models (a) and (b), respectively, from [102] they report [26]

$$J_2^{\rm Heli} = 2.201; \qquad J_4^{\rm Heli} = -5.601 \times 10^{-2}, \tag{6}$$

$$J_2^{\rm Heli} = 2.198; \qquad J_4^{\rm Heli} = -4.805 \times 10^{-2}. \tag{7}$$

In contrast, $J_2^{\rm Opt}$ in Eq. (5) follows from setting J_4 to zero, so that J_4's size indicates the size of the theoretical systematic error in that procedure. The outcome of [26] is reported as $J_2^{\rm Heli} = 2.20 \pm 0.03$ by [32] and results from combining all the J_2's in Table II of [26] (including a uniform solar rotation result) [103]. The update of the 2004 analysis by [101] reports J_{2n} with $n = 1 \ldots 5$ using data from either the Helioseismic and Magnetic Imager on the Solar Dynamics Observatory (SDO/HMI) or SoHO/MDI using the online compilation of [104] with the analysis of [105,106], upon the use of either the CESAM [107] or ASTEC [108] theoretical (solar evolution) frameworks. With CESAM, they report [101]

$$\text{SDO/HMI:}\ J_2^{\rm Heli} = 2.211; \qquad J_4^{\rm Heli} = -4.252 \times 10^{-2}, \tag{8}$$

$$\text{SoHO/MDI:}\ J_2^{\rm Heli} = 2.204; \qquad J_4^{\rm Heli} = -4.064 \times 10^{-2}. \tag{9}$$

Using ASTEC, they find [101]

$$\text{SDO/HMI:}\ J_2^{\rm Heli} = 2.216; \qquad J_4^{\rm Heli} = -4.256 \times 10^{-2}, \tag{10}$$

$$\text{SoHO/MDI:}\ J_2^{\rm Heli} = 2.208; \qquad J_4^{\rm Heli} = -4.069 \times 10^{-2}. \tag{11}$$

The data sets SDO/HMI and SoHO/MDI are independent and correspond to observations from 2010 April–2020 July and 1996 May–2008 March, respectively. The slight differences in the reported outcomes of the two data sets could stem from a time dependence [101,109] or from an observational systematic error that differentiates between the two instruments or both. We note that the SDO/HMI and MESSENGER results are roughly contemporaneous. Computing the average and standard deviation of the results using one data set or the other, we find

$$\text{SDO/HMI:}\ J_2^{\rm Heli} = 2.214 \pm 0.002, \quad J_4^{\rm Heli} = (-4.254 \pm 0.002) \times 10^{-2}, \tag{12}$$

$$\text{SoHO/MDI:}\ J_2^{\rm Heli} = 2.206 \pm 0.002, \quad J_4^{\rm Heli} = (-4.067 \pm 0.003) \times 10^{-2}. \tag{13}$$

Here, the error stems entirely from the use of different solar models. We note that the midpoints of the observing periods for the SDO/HMI and SoHO/MDI data sets are separated by 11 years, where J_2 changes by $|\Delta J_2^{\rm Heli}| = 0.008 \pm 0.002$, since the errors are not independent. For reference, Antia *et al.* [110] use the SoHO/MDI data to find a J_2 of 2.220 ± 0.009, where the error denotes the estimated time dependence [110]. Given this, we suppose that $|\Delta J_2^{\rm Heli}|$ could indeed stem from time dependence, rather than from an observational systematic error. We thus employ $J_2^{\rm Heli}$ in Eq. (12), using SDO/HMI data, as the helioseismological outcome to be compared with orbital determinations of J_2 from the MESSENGER data, because they are approximately contemporaneous. Using the $J_2^{\rm Orb}$ result of [32] that assumes GR, we find a small, albeit significant, difference in the assessment of J_2 from orbital and solar measurements,

$$J_2^{\rm Orb}|_{\beta=1;\eta=0} - J_2^{\rm Heli} = 0.057 \pm 0.006(\pm 0.020), \tag{14}$$

where the error in parentheses replaces the value of ± 0.006 if the estimated error in Earth's orbit [95] is taken into account. Of course, the error in $J_2^{\rm Heli}$ in Eq. (12) that appears in these differences come from the use of different solar models, a systematic error of theoretical origin that may be underestimated, and we can wonder about how else to estimate it. Alternatively, we estimate the error in $J_2^{\rm Heli}$ by using all four values in Eqs. (12) and (13) demanding that $\chi^2 = 1$ for a flat-line fit. This gives an average $J_2^{\rm Heli}$ of 2.210 ± 0.004, so that Eq. (14) becomes 0.061 ± 0.009. Separately, as we detail in Appendix B, if we compute an average and standard deviation of our collected helioseismological results, we find

$$\langle J_2^{\rm Heli} \rangle|_{\rm all} = 2.213 \pm 0.002, \tag{15}$$

which, interestingly, is also consistent with Eq. (12).

Since the assessment of the solar quadrupole moment from helioseismology, $J_2^{\rm Heli}$, is key to our analysis, we pause to consider the parameters on which it depends. The solar models employed are calibrated to precise helioseismic data, including the Sun's internal sound-speed profile, rotation, and composition. They appear to be robust: variations in the composition, the equation of state, or the internal rotation typically change J_2 by less than 1% [26,111]. Recent work confirms and tightens this assessment, with solar models differing in composition or opacity yielding J_2 values that vary by $\lesssim 0.2\%$ [101]. We note that the integral that yields J_2 has significant support in the radiative zone, where helioseismic constraints permit little variation [101]. For instance, Mecheri and Mertah [101] found that including differential rotation in the convection zone shifts J_2 by only about 0.5%, while changes to core conditions produce even smaller deviations. In contrast, the central discrepancy we identify between the orbital determinations (e.g., $J_2^{\rm orb} \simeq 2.27$–$2.28$ [31,32] in the GR limit) and the helioseismic value ($J_{2,\rm helio} \simeq 2.21$) is $\simeq 0.06$, which is several times larger than the spread determined from the noted modeling uncertainties. Nevertheless, since the size of the observed discrepancy challenges explanation by modeling assumptions alone, this suggests that further investigation of its possible limitations is both justified and necessary.

The significance of the result in Eq. (14) also relies, however, on assuming GR values for the PPN parameters β and η, although this is the usual procedure if the possibility of dark matter is considered. Finally, referring to the Tables in Appendix B, we observe that each of the modern $J_2^{\rm Heli}$ assessments (after 1990) are numerically smaller than those relying on MESSENGER data [31,32], even without assuming GR, though not all are significantly so. The tabulated values of the optical J_2 computed from the observed oblateness show that the errors are much larger, so that a similar comparison with the orbital results is not possible. We also show alternate orbital J_2 assessments in Appendix B. Analyses in which the ELT effect is taken into account and the various PPN parameters are fitted are arguably better and give a plausibly more robust inference of J_2 than studies that do neither. The three different methods we have considered to assess J_2 probe the Sun's shape, but they are also sensitive to different mass distributions. Their difference can limit the presence of additional matter within Mercury's orbit, as we discuss next.

VI. LIMITS ON MASS AND DISTRIBUTION OF NONLUMINOUS MATTER

Disagreements in the assessment of nominally equal quantities, as we have noted for J_2, can signal the presence of nonluminous matter within Mercury's orbit. If that matter were a spherical dark matter halo, then we would expect its presence to reduce $J_2^{\rm Orb}$ with respect to visible assessments, yielding

$$J_2^{\rm Orb} < J_2^{\rm Opt}, J_2^{\rm Heli}. \tag{16}$$

On the other hand, if a dark disk coplanar with the planetary orbits was present, then we would expect, rather,

$$J_2^{\rm Orb} > J_2^{\rm Opt}, J_2^{\rm Heli}. \tag{17}$$

We can also use the differences in the J_2 assessments to limit the excess mass enclosed, as we determine later in this section. Observational limits can also be placed on the change in the Sun's mass with time, namely, $\dot{M}_\odot$, but, as we have noted, the current limit is less than the changes expected from dust deposition or mass loss through the action of the solar wind [32]. Also, we can limit the possibility of unexpected gravitational perturbations on Mercury's orbit. Finally, since we have a "visible" assessment of J_2 determined in two different ways, we can also use Eq. (2) to back out a limit on the odd J_n moments. We note that J_{2n+1} can be a signed quantity.

We now work through these points in reverse order. To determine a limit on the odd J_n moments, we combine $\Delta_\odot$ from Fivian *et al.* [91], which is from 2008, with the roughly contemporaneous assessment using SoHO/MDI data from Mecheri and Meftah [101], averaged over solar models, as reported in Eq. (13). With this, using Eq. (2) and $\Delta r_{\rm surf}/R_\odot$ for its last term, as in [91], we thus find

$$J_1 + J_3 \simeq J_1 = -1.1 \pm 1.5. \tag{18}$$

We note that J_1 can easily be larger than J_3 because it can be generated by either external forces on the Sun or by a shift of the solar c.m. from its visible one. Although J_1 is consistent with zero, it is intriguing that its central value obeys $J_1 < 0$, which is compatible with the Sun's location north of the Galactic midplane. We recall that the inverse-square-law nature of gravitational forces ensures that the acceleration of a star is typically determined by the mass distribution at large scales, rather than by stars in its immediate vicinity [112].

Now we turn to the question that motivates this paper: how the amount of nonluminous mass, supposing some distribution, is limited through the different determinations of J_2. The constraints we develop in this section concern limits on the approximate total mass within Mercury's orbit. For reasons of simplicity, we consider the possibility of a dark disk or ring in the plane of Mercury's orbit and a spherical dark halo all centered on the Sun's c.m., though some mixture of these, or some more complicated shape, could also be possible. We have noted that dust studies point to the existence of a dusty ring coinciding with the average path of Mercury's orbit [18], and our studies limit its possible mass, but not just. Since dust, or conventional matter more generally, could act as a substrate for the

ultralight dark-matter capture mechanism described in [67], or that other dark-matter enhancement mechanisms could operate, dark matter, i.e., nonstandard, nonluminous matter, could also contribute appreciably to the nonluminous mass within Mercury's orbit. We note that the most precisely determined J_2 values, as in Eq. (14), may differ fairly significantly from zero, suggesting that Eq. (17) holds and a nonluminous disk is favored. Nevertheless, in what follows, we suppose either a disk/ring or spherical halo scenario and limit the associated mass with each.

A. Limiting the mass of a nonluminous disk or ring

We conceptualize this object as an axially symmetric circumsolar ring potentially composed of both dust and dark matter, centered about the c.m. of the visible Sun. It is characterized by a mass M_r, a uniform density σ, an inner radius R_i, an outer radius R_o, and a height h along the $\hat{\mathbf{z}}$-axis, defined as perpendicular to the plane of Mercury's orbit, noting that the Sun's rotation axis, at epoch 1950.0, is tilted about 3.38° with respect to it [4]. In what follows, though, we set that tilt to zero for simplicity. To compute its gravitational quadrupole moment, we assume the ring is also rigid. In a Cartesian coordinate system, the moment of inertia tensor is diagonal, and [113]

$$J_2^{\rm ring} = \frac{1}{M_{\rm r}\bar{R}^2}(I_z - I_x), \tag{19}$$

with $\bar{R} \equiv (R_i + R_o)/2$, where the moment of inertia in the direction s is given by

$$I_s = \int d^3r\, \rho(\mathbf{r})[r^2 - (\mathbf{r}\cdot\hat{\mathbf{e}}^{(s)})^2]. \tag{20}$$

More concretely,

$$I_z = \frac{M_{\rm r}}{2}[R_o^2 + R_i^2], \tag{21}$$

$$I_x = M_{\rm r}\left[\frac{1}{4}(R_o^2 + R_i^2) + \frac{h^2}{12}\right], \tag{22}$$

and thus,

$$J_2^{\rm ring} = \frac{1}{\bar{R}^2}\left[\frac{1}{4}(R_o^2 + R_i^2) - \frac{h^2}{12}\right]. \tag{23}$$

Combining the potential of the dust ring with the Sun's for $r > R_o$, Eq. (1), yields

$$\phi_o^{\rm tot} = \frac{M_\odot + M_{\rm r}}{r} - \left(\frac{J_2^{\rm int} M_\odot R_\odot^2 + J_2^{\rm ring} M_{\rm r}\bar{R}^2}{r^3}\right) \times \left(\frac{3\cos^2\theta - 1}{2}\right), \tag{24}$$

where $J_2^{\rm int}$ is the intrinsic solar quadrupole moment, which may be measured through a direct optical measurement or via helioseismology. Defining the fractional mass of the ring, $\epsilon_{\rm r} \equiv M_{\rm r}/M_{\rm tot}$, with $M_{\rm tot} \equiv M_\odot + M_{\rm r}$, the extrinsic solar quadrupole moment ($J_2^{\rm ext}$), which can be measured gravitationally, becomes

$$\begin{aligned} J_2^{\rm ext} &= (1-\epsilon_{\rm r})J_2^{\rm int} + \epsilon_{\rm r}\left(\frac{\bar{R}}{R_\odot}\right)^2 J_2^{\rm ring} \\ &= (1-\epsilon_{\rm r})J_2^{\rm int} + \epsilon_{\rm r}\left(\frac{1}{R_\odot^2}\right)\left[\frac{1}{4}(R_o^2 + R_i^2) - \frac{h^2}{12}\right], \end{aligned} \tag{25}$$

which can be solved for $\epsilon_{\rm r}$,

$$\epsilon_{\rm r} = \frac{2(J_2^{\rm ext} - J_2^{\rm int})}{(R/R_\odot)^2 - 2J_2^{\rm int}}, \tag{26}$$

where

$$R \equiv \sqrt{\frac{R_o^2 + R_i^2}{2} - \frac{h^2}{6}}. \tag{27}$$

This reduces to $R = R_i = R_o$ for a very thin ring of negligible height, $h/R_i \approx 0$. Here, we assume $h/R_i \ll 1$ and note $R_i \geq R_\odot$. Defining $\delta J_2 \equiv J_2^{\rm ext} - J_2^{\rm int}$, we rewrite Eq. (26) as

$$\frac{\delta J_2}{J_2^{\rm int}} = \epsilon_{\rm r}\left[\frac{1}{2J_2^{\rm int}}\left(\frac{R}{R_\odot}\right)^2 - 1\right] \approx \epsilon_{\rm r}\left[\frac{1}{2J_2^{\rm int}}\left(\frac{R}{R_\odot}\right)^2\right]. \tag{28}$$

Recalling [18] and thus the ring's proximity to Mercury's orbit with $R_o \approx R_i \approx 0.38$ A.U., we estimate

$$\frac{\delta J_2}{J_2^{\rm int}} \approx \epsilon_{\rm r}(1.5\times 10^{10}), \tag{29}$$

implying that a 1% difference in J_2, that is, $\delta J_2 \sim 10^{-2} J_2^{\rm int}$, could be caused by $M_{\rm r} \sim 10^{-12} M_\odot$. Such a mass can contain a dark-matter component, though its value corresponds to that of a relatively large asteroid, significantly more massive than those more commonly found in the asteroid belt. We note, however, the dwarf planet Ceres, the most massive known object in the asteroid belt between Mars and Jupiter, has a mass of about $5\times 10^{-10} M_\odot$, whereas Jupiter's moon Amalthea has a mass of about $(1.04 \pm 0.08)\times 10^{-12} M_\odot$ [114]. We now turn to concrete limits.

Given determinations of $J_2^{\rm ext}$ from orbital measurements $J_2^{\rm Orb}$ and of $J_2^{\rm int}$ from both optical and helioseismological measurements $J_2^{\rm Opt}$ and $J_2^{\rm Heli}$, we constrain the mass in a circumsolar ring or disk through limits on ϵ_r in Eq. (26). Since we assign $M_\odot$ to mass within $R_\odot$, practically $R/R_\odot > 1$, and since $J_2 \sim \mathcal{O}(10^{-7})$, we write

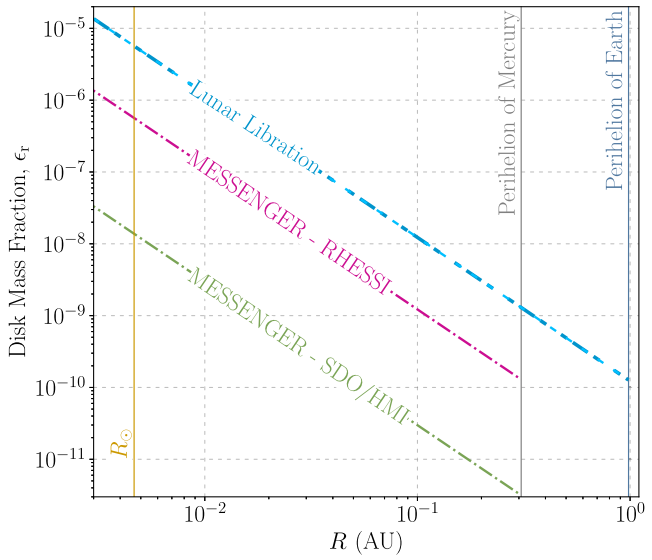

FIG. 1. Limits at 95% C.L. (2σ) on the maximum mass fraction, $\epsilon_r \equiv M_r/M_{tot}$, of a dark matter/dust ring or disk around the Sun, derived from the difference in gravitational and optical/helioseismological determinations of the gravitational quadrupole moment J_2 as in Eq. (30), noting the maximum values of δJ_2 at 2σ in Eqs. (31) and (32), plotted as dashed lines. The horizontal axis, R, is determined by the geometric dimensions of the dark matter/dust ring or disk, as defined in Eq. (27). The dashed line corresponds to constraints inferred from the lunar libration limit on J_2^{ext} [115]. We refer to the text for all details.

$$\epsilon_r = 2\left(\frac{R_\odot}{R}\right)^2 \delta J_2, \tag{30}$$

so that our ability to determine δJ_2 limits the maximum mass in the ring, regardless of our confidence that $\delta J_2 > 0$. We compute the maximum value of ϵ_r at 95% C.L. through different evaluations of the maximum value of δJ_2 at 2σ, and we display the results in Fig. 1, noting that R can range from within $R_\odot$ to the location of Mercury's orbit.

To accomplish this, we use J_2^{Orb} derived from the latest MESSENGER analysis [32], given in Eq. (4). This is then combined with either optical [91], as shown in Eq. (5), or helioseismological measurements [101], noted in Eqs. (8) and (10). With the most significant difference, given in Eq. (14) (noting that if the enlarged error were used the allowed mass would be larger), we have

$$\max(\delta J_2)|_{2\sigma} = 0.069, \tag{31}$$

whereas combining Eq. (4), using either the $\beta = 1$; $\eta = 0$ constrained (GR) or unconstrained value, with the optical result of Eq. (5) yields

$$\max(\delta J_2)|_{2\sigma} = 2.82(2.83), \tag{32}$$

respectively. We report the limits on ϵ_r with R at 95% C.L. (2σ) that come out, using the GR-constrained orbital result in Fig. 1. Furthermore, we also depict the constraint on ϵ_r that follows from the limit $J_2^{ext} < 3 \times 10^{-6}$ [115], determined by demanding that the lunar librations, which are modeled and observed from the analysis of lunar laser ranging (LLR) measurements of the Earth-Moon distance [116], do not exceed $3\sigma/2$ of the LLR residuals. We note that this limit is sufficiently weak that the impact of the use of J_2^{Opt} in Eq. (5) or J_2^{Heli} from combining Eqs. (8) and (10) is indistinguishably small.

Thus far, we have limited ϵ_r supposing that a dark disk or ring exists. Now, we assess the likelihood of this scenario using Eq. (17) and the observed values of J_2^{ext} and J_2^{int}. Adopting a Gaussian prior for δJ_2, the relevant posterior probability is given by [117]

$$P(\delta J_2 > 0 | J_2^{ext}, J_2^{int}) = 1 - F_{\delta J_2}(z), \tag{33}$$

where $F_{\delta J_2}(z)$ is the cumulative distribution function (CDF) of the standard normal distribution,

$$F_{\delta J_2}(z) = \frac{1}{\sqrt{2\pi}} \int_z^\infty dt\, \exp(-t^2/2), \tag{34}$$

and $z = -\mu_{post}/\sigma_{post}$. Here, μ_{post} and σ_{post} are the posterior mean and standard deviation, respectively. For a noninformative (flat) prior where the standard deviation of the prior (σ_{prior}) tends towards infinity, μ_{post} and σ_{post} simplify to yield

$$z \approx \frac{\mu_{J_2^{int}} - \mu_{J_2^{ext}}}{\sigma_{J_2^{ext}} + \sigma_{J_2^{int}}}. \tag{35}$$

The deviation of the computed posterior probabilities, as formulated in Eq. (33), from one are presented for six distinct cases in Table I. We observe that even in the unconstrained cases that the probability that a disk exists is high, although our concern regarding solar model uncertainties remains. Please note "Ext" refers to "Extrinsic" and "Int" refers to "Intrinsic", whereas "Opt", "Heli," and "Heli-All" are defined through the equations referenced in the caption.

TABLE I. The deviation of the disk structure's presence likelihood from one, $1 - P(\delta J_2 > 0)$, evaluated using Eq. (33). We compared the GR-constrained (unconstrained) J_2^{ext} values from MESSENGER data, as given by Eq. (4), against the best optical and helioseismological determinations of J_2^{int}, given by Eqs. (5), (12), and (15), respectively. We refer to the text for all details.

	Ext	
Int	Constrained	Unconstrained
Opt	0.210	0.221
Heli	1.0×10^{-21}	0.091
Heli-All	2.4×10^{-17}	0.089

B. Limiting the mass of a nonluminous spherical halo

For a spherical halo, setting $J_2^{\rm ring} = 0$ in Eq. (25) yields

$$\epsilon_{\rm s} = \frac{J_2^{\rm int} - J_2^{\rm ext}}{J_2^{\rm int}}, \tag{36}$$

in which we denote the fractional mass of the spherical halo by $\epsilon_{\rm s} \equiv M_{\rm s}/M_{\rm tot}$. We apply the Feldman-Cousins [118] method to establish limits on $\epsilon_{\rm s}$ given pairs of $(J_2^{\rm ext}, J_2^{\rm int})$ values. The resulting limit on $\epsilon_{\rm s}$, derived by comparing the constrained (unconstrained) MESSENGER $J_2^{\rm ext}$ values in Eq. (4) with $J_2^{\rm Heli}$ from Eq. (12), is given by

$$\epsilon_{\rm s}|_{2\sigma} = 2.5 \times 10^{-4}(8.3 \times 10^{-3}). \tag{37}$$

We now take the existence of Mercury's circumsolar dust ring into account [20]. The portion of the dust ring that falls within the orbit of Mercury would increase $J_2^{\rm ext}$, such that Eq. (36) changes to

$$\epsilon_{\rm s} = \frac{(1-\epsilon_r)J_2^{\rm int} - J_2^{\rm ext} + (\epsilon_r/2)(R/R_\odot)^2}{J_2^{\rm int}}, \tag{38}$$

which would weaken the bounds on ϵ_s in Eq. (37) as shown in Fig. 2, where we set the dust ring's radius to $R \approx 0.31$ A.U.

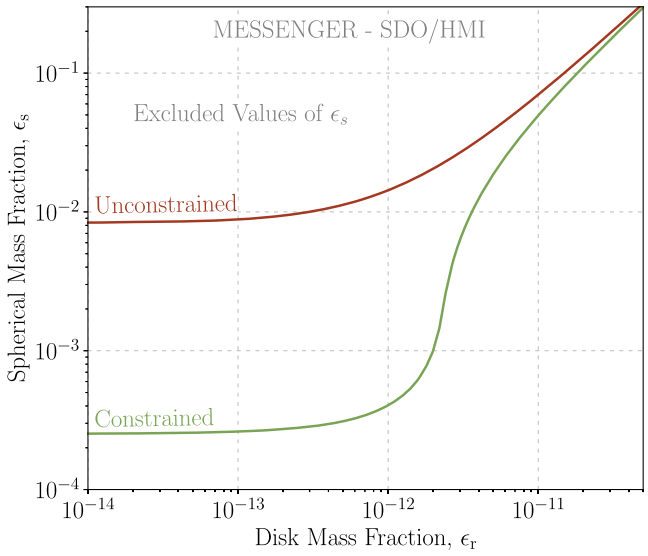

FIG. 2. Limits at 95% C.L. (2σ) on the mass fraction of a spherical dark matter halo surrounding the Sun, denoted as $\epsilon_{\rm s} \equiv M_{\rm s}/M_{\rm tot}$, plotted against the mass fraction, $\epsilon_{\rm r} \equiv M_{\rm r}/M_{\rm tot}$, of a dust ring orbiting within Mercury's path. We input the values from Eqs. (4) and (12) into Eq. (38). The GR-constrained and unconstrained cases are shown in green and red, respectively. We refer to the text for all details.

VII. IMPLICATIONS FOR DARK-MATTER MODELS

We have found that existing determinations of $J_2^{\rm Heli,Opt}$ ($J_2^{\rm int}$) and $J_2^{\rm Orb}$ ($J_2^{\rm ext}$) from the MESSENGER mission favor the existence of a nonluminous disk within Mercury's orbit, with Table I providing the likelihood that it does *not* exist. Although the significance of our claim depends on the results we pick, the limits we have found on its mass, as shown in Fig. 1, grossly exceed the contributions we would expect from the cosmological dark matter density and/or the dust ring that has been discovered near the path of Mercury's orbit [18]. The observed dust ring, assessed at an overdensity of ≈3–5% [18], is estimated to be located between heliocentric distances (radii) of 0.356271 A.U. and 0.400308 A.U., with a mass of $(1.02\text{–}4.05) \times 10^{12\pm(\approx 1)}$ kg [20]. Dust, in grains ranging in size from some 10 (100) μm to 1 cm in diameter with a density of 2000 kg/m^3, is generally an expected component [20]. Dust within our Zodiacal Cloud is observed to be depleted very close to the Sun [119], and we follow [20] in assuming this effect can be neglected beyond a radius of 0.05 A.U. to estimate that the mass in dust within Mercury's orbit to be no more than about $7 \times 10^{15\pm(\approx 1)}$ kg, or $3 \times 10^{-15\pm(\approx 1)} M_\odot$. This is still a few orders of magnitude smaller than our most stringent bound on the maximum mass within the nonluminous disk, though we can expect other massive objects to appear as well. For example, a spherical object of the same composition as dust with a radius of 2.5 km would have a mass of 1.3×10^{14} kg, so that some 100 of them would be needed to contribute a mass of 10^{16} kg, crudely comparable to that in dust. We note the Solar System survey from *Gaia* Data Release 3 reveals 432 near-Earth objects with a diameter of 5 km or less [120], though the total number and mass of such objects within Mercury's orbit is unknown. Much lighter objects, such as micrometeroids and others, may also appear in an appreciable way [45,46]. Thus, there could well be missing matter, of differing origins, within Mercury's orbit, and we now turn to how some measure of it could be *dark matter*.

The cosmic dark-matter density contributes only $10^{-19} M_\odot$ of the mass within Mercury's orbit, and local effects could modify that total mass. For example, a macroscopic dark object, such as a PBH, could exist. Interestingly, in the mass range of $(10^{-15}\text{–}10^{-11}) M_\odot$, PBHs could constitute all of the dark matter [73], though x-ray studies can offer further constraints [121]. Nevertheless, a PBH in the expected mass range could be in transit through (or contained within) the Solar System within Mercury's orbit, where we note [74] for Solar System transit rate estimates.

Ultralight dark matter could also play a role. To that end, we consider the generic halo formation mechanism of [67], arising from dark-matter self-interactions in the gravitational field of a massive celestial body, such as the Sun.

We note that ultralight dark matter models with a particle mass of $10^{-23}\ \text{eV} < m < 10^{-17}\ \text{eV}$ can produce dense solitonic cores in the Galactic Center, in which case the particle mass is constrained by the observation of the motion of the star S2 [122]. However, these constraints do not apply to the models considered here. The gravi-atom picture is promising in that a strong enhancement of the dark-matter density is possible in particular regions of parameter space; for example, this model can yield a spherical halo about the Sun with an overdensity of $\delta\rho_{\rm dm} \equiv \rho_{\rm crit}(0)/\rho_{\rm dm} \simeq 7 \times 10^3$ for an axion dark-matter candidate with a mass of 10^{-14} eV and an axion decay constant of 5×10^7 GeV, with the self-interaction strength λ given by $\lambda = -m^2/f_a^2$. The estimated extra mass this halo contributes within Mercury's mean orbit is more than 50 times smaller [67] than the "extra mass" ephemerides constraint of $\rho_{\rm dm} < 9.3 \times 10^{-18}\ \text{g/cm}^3$ [86], which yields an enclosed mass of $< 7 \times 10^{12}$ kg if $\rho_{\rm dm}$ were uniform. The constraint of [86] includes a solar J_2 of a suitable size and error [123], so that this mass limit is not at odds with our own analysis. Nevertheless, the spherical symmetry of this dark halo is at odds with the evidence we have found for an extended disklike object. However, we can adapt the gravi-atom mechanism [67] to our case by noting that the central mass M need only be much more massive than that of the dark-matter candidate m, with a halo of radius R_* that exceeds that of the central mass. Particularly, we evaluate the possibility that halos form around clumps of conventional matter in the disk, possibly yielding a number of $\ll 1$ A.U.-sized halo states. The total dark mass in the disk would then be given by the sum of the masses associated with each of the halo bound states.

Translating the gravi-atom estimates in M and m to kg and eV scales is possible because the size of the bound state, as well as the possible overdensity, are each determined by Mm^2, where $M_\odot(10^{-14}\ \text{eV})^2 \approx 200\ \text{kg eV}^2$. Here, successful halo formation in the gravi-atom picture requires a suitably sized R_*, a wavelike dark-matter candidate so that the de Broglie wavelength $\lambda_{\rm dB}$ exceeds the dark matter interparticle spacing, and a maximum halo density $\rho_{\rm crit}$ (at its center) that significantly exceeds $\rho_{\rm dm}$ ($\delta\rho_{\rm dm} \gg 1$). There are also dynamical considerations, in that dark-matter capture should exceed stripping, making $\xi_{\rm foc} \equiv \lambda_{\rm db}/R_* \gtrsim 1$, with the density reaching $\rho_{\rm crit}$ within about 5 Gyr, the lifetime of the Solar System [67]. There are also independent constraints on the axion from direct searches if it couples to photons or nucleons, and a favored parameter space of $m \in (0.7\text{–}700)\ \mu\text{eV}$ with $f_a \in (2 \times 10^{13}\text{–}2 \times 10^{10})$ GeV, if it ought also solve the strong CP problem of QCD [124]. Thus, the solar halo suggested in [67] is unlikely to be generated by a QCD axion, nor can that axion couple to photons. These features continue to bear out in the examples to which we now turn.

Different sorts of constituents could potentially act as the nucleus of a small dark-matter halo. Dust, for example, is thought to exist in grains ranging in size from some 10 (100) μm to 1 cm in diameter with a density of 2000 kg/m^3 [20], and larger clumps of matter should also occur. Here, we explore different scenarios for dark-halo formation, considering central masses comprising (i) a small asteroid with $M = 1.3 \times 10^{14}$ kg (a 2.5 km-radius rock of density 2000 kg/m^3), (ii) a much-denser asteroid with $M = 10^{16}$ kg, or (iii) Mercury itself with $M = 3.3 \times 10^{23}$ kg, with a radius of 2440 km, so that R_* must be larger than the noted radius in each case. In these cases $M \ll M_\odot$, and we might suppose an initial encounter of a dark-matter particle with the Sun produces a population of dark-matter particles that satisfy $v \ll v_{\rm halo} \approx 240$ km/s. We do not think it is possible to generate gravi-atoms with dust grain cores so that $\xi_{\rm foc} \gtrsim 1$ is satisfied.

As detailed in Appendix C, the chosen scenarios for M can satisfy the noted constraints under the following conditions: (i) $M = 1.3 \times 10^{14}$ kg, $m = 1.0 \times 10^{-2}$ eV, $f_a = 1.0 \times 10^1$ GeV for which the radius of the ground state is $R_* = 4.0$ km; the gravitational fine-structure constant $\alpha = 4.9 \times 10^{-9}$, and the dark-matter self-coupling is $\lambda = 1.0 \times 10^{-24}$, and the estimated maximum overdensity is $\delta\rho_{\rm dm} = 1.2 \times 10^6$. If this can be attained, then $M_{\rm enc,max} \approx \delta\rho_{\rm dm}\rho_{\rm dm}4\pi R_*^3/3 = 2.4 \times 10^{-4}$ kg. If $v_{\rm halo}$ characterizes the dark-matter particle speed, then

$$\xi_{\rm foc} = 3.8 \times 10^{-5}; \qquad \tau_{\rm rel} = 9.1 \times 10^8\ \text{Gyr}, \quad (39)$$

but with $v \approx 8$ m/s (just for illustration), $\xi_{\rm foc} \to 1.1$, and $\tau_{\rm rel} \to 1.0$ Gyr. However, we do not think there would be enough rocks *in situ* for this solution, if attainable, to generate a significant contribution to the disk mass.

We compare this to a heavier object that is six-times denser, finding (ii) $M = 1.0 \times 10^{16}$ kg, $m = 6.0 \times 10^{-5}$ eV, $f_a = 1.0 \times 10^1$ GeV for which the radius of the ground state is $R_* = 1.5 \times 10^3$ km, the gravitational fine-structure constant $\alpha = 2.3 \times 10^{-9}$, and the dark-matter self-coupling $\lambda = 3.6 \times 10^{-29}$. Here, $\delta\rho_{\rm dm} = 9.6$ and $M_{\rm enc,max} \approx 8.8 \times 10^{-2}$ kg with

$$\xi_{\rm foc} = 1.8 \times 10^{-5}; \qquad \tau_{\rm rel} = 2.0 \times 10^2\ \text{Gyr}, \quad (40)$$

using $v_{\rm halo}$. By making the central mass denser, we see that more mass can be stored in the halo, but here, too, it would not seem possible to generate a significant contribution to the disk mass.

Finally we consider the possibility of a halo about Mercury itself, and we consider (iii) $M = 3.3 \times 10^{23}$ kg, $m = 9 \times 10^{-11}$ eV, $f_a = 1.0 \times 10^7$ GeV so that $R_* = 0.13$ A.U., $\alpha = 1.1 \times 10^{-7}$, $\lambda = 8.1 \times 10^{-53}$. Here, $\delta\rho_{\rm dm} = 5.3 \times 10^4$ and $M_{\rm enc,max} \approx 1.2 \times 10^{15}$ kg with

$$\xi_{\rm foc} = 8.7 \times 10^{-4}; \qquad \tau_{\rm rel} = 6.6 \times 10^8\ \text{Gyr}, \quad (41)$$

for $v_{\rm halo}$, and if $v \approx 180$ m/s, $\xi_{\rm foc} \to 1.2$, and $\tau_{\rm rel} \to 3.7 \times 10^2$ Gyr, and the dynamical constraints can be reasonably well satisfied. In this case, a contribution to the mass of the disk could be as large as 6×10^{14} kg, though a deviation from sphericity, presumably from gravitational focussing, would be needed to impact the perihelion precession. Nevertheless, it appears possible to generate macroscopic contributions to a nonluminous disk from ultralight dark matter, even if we have not yet found an example through which it can grossly dominate the expected nonluminous mass.

VIII. SUMMARY

In this paper, we have considered different determinations of the Sun's gravitational quadrupole moment J_2, carefully comparing optical assessments of the Sun's shape with interferences from orbital observations, particularly using MESSENGER studies of Mercury. The pattern of observations, considered broadly, favor the pattern

$$J_2^{\rm Orb} > J_2^{\rm Opt}, J_2^{\rm Heli}, \tag{42}$$

given in Eq. (17), which speaks to the existence of a nonluminous disk. Particularly, if we compare the orbital results assuming GR and using MESSENGER data [32], Eq. (4), with contemporaneous helioseismological results from a space-based observatory [101], Eq. (12), we find the difference, given in Eq. (14),

$$J_2^{\rm Orb}|_{\beta=1;\eta=0} - J_2^{\rm Heli} = 0.057 \pm 0.006(\pm 0.020), \tag{43}$$

is greater than zero with a significance of $\simeq 3\sigma$. We have also explored how alternative helioseismological error estimates and outcomes impact this conclusion, and we find support for a significantly positive result. Consequently, we have developed constraints on the total mass and mass distribution of that nonluminous disk, and we claim that the 2σ limit on its maximum mass is no less than some $10^{-12} M_\odot$, where increasing the error in the J_2 difference gives rise to a larger maximum-mass limit. We have also carefully considered its possible components, and we found that the missing (nonluminous) mass is sufficiently large that conventional sources of mass, from dust, from asteroids and meteroids of all sizes, would not seem able to explain it. We also believe the total mass of these various components to be poorly determined. We nevertheless suppose that dark matter could also contribute to its mass. Thus, our study points to a possible "missing mass" problem within Mercury's orbit. A macroscopic dark matter candidate, such as a PBH of a mass typical of an asteroid, is one concrete possibility. We have also considered how a particular ultralight dark matter model with self-interactions [67] can generate a massive dark halo about Mercury itself, potentially contributing to the appearance of a massive ring in the path of Mercury's orbit.

We anticipate that the BepiColombo mission to Mercury, to arrive in 2025, can refine the results from the earlier MESSENGER mission, that we have exploited in this paper, with further precision measurements of Mercury's orbit and magnetic properties offering the prospect of confirming and refining our findings—or not. Particularly, precise assessments of short timescale perturbations on Mercury's orbit should constrain massive exotic objects in transit through the Solar System, such as the PBHs candidates discussed in [74]. Although the dark-matter particles we have particularly considered would not seem to be axions, we expect that magnetic field studies may well be discriminating nonetheless, as they can probe the possibility of macroscopic dark-matter objects with a slight electric charge. Additional studies of dust are also planned [125]. Ultimately, too, we expect these studies to have implications for the precision of future relativistic general relativity tests [24].

To confirm and refine our findings we emphasize that the following probes are possible in the near future:

(i) Detected perturbations in Mercury's orbit can speak to the existence of ultraheavy dark matter.
(ii) Studies of light reddening in the inner Solar System can be used to separate a dusty, nonluminous component from dark matter.
(iii) The JUNO neutrino experiment is poised to measure CNO neutrinos [126] with higher precision than BOREXINO and can test the latter's inference of a nonhomogeneous zero-age Sun, which supports the existence of an early protoplanetary disk, some of which may still remain.

Thus we are hopeful that the possible "missing mass" problem we have uncovered can be clarified in the relatively near future.

ACKNOWLEDGMENTS

We thank Lance Dixon, Antonio Genova, Roni Harnik, Dan Hooper, Russell Howard, Mrunal Korwar, and Guillermo Stenborg for helpful correspondence and comments, and we are grateful to the anonymous referee for bringing the work of [95] to our attention. S. G. would like to thank the Theoretical Division at Fermilab for lively hospitality and to acknowledge the Universities Research Association for support during a sabbatical visit in which this project was initiated. G. F. S. A. would like to thank the hospitality of the Fermilab Theory Group. G. F. S. A., P. M., and M. Z. are grateful to the Center for Theoretical Underground Physics and Related Areas (CETUP*), The Institute for Underground Science at Sanford Underground Research Facility (SURF), and the South Dakota Science and Technology Authority for their hospitality and financial support. That stimulating environment was invaluable to us. S. G. and M. Z. also acknowledge support from the U.S. Department of Energy, Office of Science, Office of Nuclear Physics under Contract

No. DE-FG02-96ER40989. P. M. is supported by Fermi Research Alliance, LLC under Contract No. DE-AC02-07CH11359 with the U.S. Department of Energy, Office of Science, Office of High Energy Physics. G. F. S. A. is fully financially supported by Fundação de Amparo à Pesquisa do Estado de São Paulo (FAPESP) under Contracts No. 2022/10894-8 and No. 2020/08096-0.

APPENDIX A: OBLATENESS AND ITS GRAVITATIONAL EFFECTS

Here, we show how a relationship between the solar oblateness and its gravitational moments can be established under the assumption that the solar surface constitutes an equipotential surface [127,128], i.e., $\Phi(R_e) = \Phi(R_p)$. Assuming further that the Sun's rotation (Ω) depends solely on the distance from its rotation axis, $l = r\sin\theta$, and disregarding magnetic stresses, the effective potential can be expressed as [29]

$$\Phi \equiv \phi_i - \phi_\Omega = \phi_i - \int_0^{l_\odot} l\Omega^2(l)dl, \qquad l = r\sin\theta, \quad \text{(A1)}$$

where ϕ_i and ϕ_Ω represent the internal potential of the Sun and the effective potential due to rotation, respectively. The continuity of the potential across the Sun's surface yields $\phi_i^{\rm surf} = \phi_o^{\rm surf}$, where ϕ_o is the gravitational potential outside the Sun, given by Eq. (1). The equipotential condition $\Phi(R_e) = \Phi(R_p)$ results in

$$\frac{\Delta_\odot}{\eta_p^2\left(1+\frac{\Delta_\odot}{\eta_p}\right)} + \sum_n \frac{J_n}{\eta_p^{n+1}}\left(\frac{P_n(0)}{\left(1+\frac{\Delta_\odot}{\eta_p}\right)^{n+1}} - 1\right) + \frac{R_\odot\phi_\Omega(R_e)}{GM_\odot} = 0, \quad \text{(A2)}$$

where $\eta_{e,p} \equiv R_{e,p}/R_\odot$, and η_e replaced by $\eta_e = \Delta_\odot + \eta_p$. Noting that $(\eta_e + \eta_p)/2 = 1 + \mathcal{O}(\Delta_\odot^2)$, η_p expanded to linear order in $\Delta_\odot$ is given by $\eta_p \approx 1 - \Delta_\odot/2$. Hence, Eq. (A2) expanded to linear order in $\Delta_\odot$ and up to the octopole moment ($n = 4$) is

$$\Delta_\odot^{(4)} = \frac{(16R_\odot\phi_\Omega(R_e)/GM_\odot) - 2(8J_1 + 12J_2 + 8J_3 + 5J_4)}{4(4J_1 + 3J_2 + 8J_3 - 4) + 55J_4}. \quad \text{(A3)}$$

Given that all the multipoles are expected to be smaller than the monopole term, $J_n \ll 1$, the oblateness in Eq. (A3) can be approximated by keeping only the linear terms:

$$\Delta_\odot^{(4)} \approx J_1 + \frac{3J_2}{2} + J_3 + \frac{5J_4}{8} - \frac{R_\odot\phi_\Omega(R_e)}{GM_\odot}, \quad \text{(A4)}$$

which in the case of a rigidly rotating body reduces to Eq. (2).

APPENDIX B: GRAVITATIONAL QUADRUPOLE MOMENTS

We have performed an extensive review of the previous determinations of the solar gravitational quadrupole moment. There are three distinct ways by which the Sun's shape can be inferred: through the optical measurement of its oblateness (Table II), through helioseismology (Table III), and through measurements of planetary orbits (Tables IV and V). We base our analysis on a few values from these tables, and we detail our motivations in doing so here. First, among the optical measurements reported in Table II, only results Nos. 14–17 take into account corrections for surface magnetism, and [91] (No. 14) provides the most precise determination to date, though we note [92] (No. 17) for further discussion of that earlier work.

The helioseismological measurements in Table III have been categorized based on the instruments used. The values reported in [101], namely, Nos. 10 and 11 and Nos. 17 and 18 in Table III figure prominently in our analysis because of their improved analysis framework and the extensive helioseismological data sets they employ. We can also consider the results for each distinct instrument and determine the average value and standard deviation for each case, to find using Table III that

$$J_2^{\rm SoHO/MDI} = 2.135 \pm 0.203, \quad \text{(B1)}$$

$$J_2^{\rm GONG} = 2.167 \pm 0.019, \quad \text{(B2)}$$

TABLE II. Summary of optical J_2 measurements. To translate from visual oblateness $\Delta_\odot$ to J_2 we use Eq. (2), including only the J_2 contribution and assuming $\Delta r_{\rm surf} = 7.78$ mas [29]. In the Reference column, we indicate the first author followed by the date(s) of observation of the corresponding measurement.

Optical J_2 measurements				
No.	$\Delta_\odot(\times10^{-6})$	$J_2(\times10^{-7})$	$\pm J_2(\times10^{-7})$	References
1	50 ± 7	279	47	Dicke, 66 [3]
2	9.6 ± 6.6	9.91	43.8	Hill, 73 [129]
3	20.0 ± 1.5	79.4	9.73	Dicke, 83 [128]
4	5.8 ± 1.4	−15.1	9.03	Dicke, 84 [5]
5	15.2 ± 2.3	47.4	15.3	Dicke, 85 [6]
6	14.4 ± 1.4	41.9	9.03	Beardsley, 83 [130]
7	5.6 ± 6.3	−16.7	42.0	Maier, 90 [131]
8	4.3 ± 2.0	−25.3	13.3	Egidi, 92 [132]
9	8.5 ± 2.1	2.67	14.0	Egidi, 93 [132]
10	8.6 ± 1.4	3.33	9.33	Egidi, 94 [132]
11	10.3 ± 1.9	14.7	12.7	Egidi, 95 [132]
12	9.0 ± 2.9	6.44	19.5	Emilio, 97 [90]
13	19.7 ± 1.9	77.3	13.2	Emilio, 01 [90]
14	8.35 ± 0.15	1.46	1.0	Fivian, 02–08 [91]
15	8.8 ± 0.3	4.3	2.1	Irbah, 11 [133]
16	8.19 ± 0.33	0.55	2.22	Meftah, 10–11 [134]
17	7.5 ± 0.5	−4.0	3.4	Kuhn, 10–12 [92]

TABLE III. Summary of helioseismological J_2 measurements. Measurements Nos. 1–3 use the rotational splitting data from [135], Nos. 4–11 use data from SoHO/MDI [105,136], Nos. 12 and 13 use data from SoHO/MDI and the ground-based Global Oscillation Network Group (GONG) [137], Nos. 14–16 use data from GONG, and Nos. 17 and 18 use data from SDO/HMI [106].

Helioseismological J_2 measurements				
No.	$J_2(\times 10^{-7})$	$\pm J_2(\times 10^{-7})$	References	Solar model
1	36	⋯	Gough [138]	[139]
2	1.7	0.4	Duvall [140]	[139]
3	55	13	Hill [141][a]	⋯[b]
4	2.23	0.09	Pijpers [36]	[142]
5	2.22	0.02	Armstrong [143]	[144]
6	1.6	0.04	Godier [145,146][c]	[147]
7	2.201	⋯	Mecheri [26]	[102][d]
8	2.198	⋯	Mecheri [26]	[102]
9	2.220	0.009	Antia [110][e]	
10	2.204	⋯	Mecheri [101]	[107]
11	2.208	⋯	Mecheri [101]	[108]
12	2.206	⋯	Roxburgh [111]	[142]
13	2.208	⋯	Roxburgh [111]	[148]
14	2.14	0.09	Pijpers [36]	[142]
15	2.18	⋯	Antia [149]	
16	2.180	0.005	Antia [110][e]	
17	2.211	⋯	Mecheri [101]	[107]
18	2.216	⋯	Mecheri [101]	[108]

[a]This is the corrected value after accounting for a missing numerical factor [4].
[b]Solar model by Saio, H. (1982), private communication [141].
[c]The uncertainty is reported in [150].
[d]Measurements 7 and 8 use models (a) and (b) for the solar differential rotation from [102], respectively.
[e]The central value and error come from the *time average* of J_2 measurements over 10 years.

$$J_2^{\mathrm{SDO/HMI}} = 2.214 \pm 0.002. \tag{B3}$$

We use these to calculate a combined average value of J_2 of these independent measurements, yielding

$$\langle J_2^{\mathrm{Heli}} \rangle|_{\mathrm{all}} = 2.213 \pm 0.002. \tag{B4}$$

Thus, we see that we recover a result compatible with Eq. (12) through completely different means, supporting our earlier analysis, albeit the HMI results have the smallest dispersion.

Lastly, for orbital determinations, we employ only the most recent J_2 analysis using MESSENGER data [32]. This work does take into account the ELT correction and makes a simultaneous fit of PPN parameters in their J_2 determination. These are important additions, and we have to make sure we are comparing J_2 assessments that take into account the same effects. Table IV serves this purpose as we opt to report only those values that consider these additions in their J_2 determination. For completeness, in Table V, we compile several orbital assessments for comparison indicating whether they included either the ELT effect, a simultaneous fit of PPN parameters, or both.

TABLE IV. Summary of orbital J_2 measurements. Measurements No. 1 and No. 2 are orbital assessments using data almost exclusively from measurements of Mercury's orbit. We also include the ephemerides analyses that have taken into account the ELT effect and fit for J_2 together with PPN parameters.

Orbital J_2 measurements			
No.	$J_2(\times 10^{-7})$	$\pm J_2(\times 10^{-7})$	References
1	2.25	0.09	Park, 11–14 [31]
2	2.246	0.022	Genova, 08–15 [32]
3	2.165	0.12	Fienga, ⋯ [151]
4	2.206	0.03	Fienga, ⋯ [151]

TABLE V. Extended summary of the orbital J_2 assessments including information as to whether the references included a simultaneous fit of the PPN parameters or the ELT effect correction in their analysis.

Orbital J_2 measurements					
No.	$J_2(\times 10^{-7})$	$\pm J_2(\times 10^{-7})$	ELT	PPN	References
1	180	200	N	N	Lieske, 49–68 [152]
2	13.9	24.7	N	Y	Shapiro, 66–71 [153]
3	25	16	N	Y	Anderson, 11–76 [154]
4	12.3	11.5	N	N	Anderson, ⋯ [123]
5	−1.8	4.5	N	Y	Eubanks, ⋯ [123]
6	−11.7	9.5	N	Y	Pitjeva, ⋯ [123]
7	−1.3	4.1	N	Y	Pitjeva, 64–89 [155]
8	2.4	0.7	N	Y	Pitjeva, ⋯ [156]
9	−5	10	N	Y	Williams, 96–00 [157]
10	6.6	9.0	N	N	Afanaseva, 80–86 [158]
11	−6	58	N	N	Landgraf, 49–87 [159]
12	2.3	5.2	N	Y	Anderson, 71–97 [160]
13	1.9	0.3	N	Y	Pitjeva, 61–03 [161]
14	2.22	0.23	N	Y	Pitjeva, ⋯ [123]
15	2.25	0.09	Y	Y	Park, 11–14 [31]
16	2.246	0.022	Y	Y	Genova, 08–15 [32]
17	2.46	0.68	N	Y	Standish, ⋯ [162]
18	2.295	0.010	N	N	Viswanathan, ⋯ [163]
19	1.82	0.47	N	N	Fienga, ⋯ [164]
20	1.8	⋯	N	Y	Konopliv, ⋯ [165]
21	2.0	0.20	N	Y	Pitjeva, ⋯ [166]
22	2.40	0.25	N	Y	Fienga, ⋯ [167]
23	2.27	0.25	N	Y	Fienga, ⋯ [168]
24	2.22	0.13	N	Y	Fienga, ⋯ [168]
25	2.165	0.12	Y	Y	Fienga, ⋯ [151]
26	2.206	0.03	Y	Y	Fienga, ⋯ [151]
27	2.40	0.20	N	Y	Verma, ⋯ [169]
28	2.010	0.010	N	N	Fienga, ⋯ [170]
29	2.2180	0.01	Y	N	Fienga, ⋯ [171]

APPENDIX C: DARK HALO FORMATION

We follow [67] to find that a gravi-atom radius is set by

$$R_* = \frac{(\hbar c)^2 c^2}{GM(mc^2)^2} \approx 0.035 \text{ A.U.} \left(\frac{10^{12} \text{ kg}}{M}\right)\left(\frac{100 \text{ μeV}}{m}\right)^2, \tag{C1}$$

noting that 0.035 A.U. $\approx 7.5 R_\odot$. The gravitational coupling α is determined by $R_* = (m\alpha)^{-1}$, and the bound-state escape velocity is $\sqrt{2}\alpha$. The associated de Broglie wavelength $\lambda_{\rm db}$ of a dark-matter particle is

$$\lambda_{\rm db} \approx 1.6 \times 10^1 \text{ m} \left(\frac{100 \text{ μeV}}{m}\right)\left(\frac{240 \text{ km/s}}{v}\right), \tag{C2}$$

where v is the particle speed. Dark matter is wavelike if $\lambda_{\rm db}$ exceeds the dark interparticle spacing, possible if $m \lesssim 30$ eV. Moreover,

$$\xi_{\rm foc} \approx 2.9 \times 10^{-9} \left(\frac{M}{10^{12} \text{ kg}}\right)\left(\frac{m}{100 \text{ μeV}}\right)\left(\frac{240 \text{ km/s}}{v}\right). \tag{C3}$$

If $\xi_{\rm foc} \gtrsim 1$, the expected maximum overdensity, with $\delta\rho_{\rm dm} \sim \rho_{\rm dm}$, is

$$\delta\rho_{\rm dm} = 7 \times 10^{13} \left(\frac{f_a}{10^{11} \text{ GeV}}\right)^2 \left(\frac{M}{10^{12} \text{ kg}}\right)^2 \left(\frac{m}{100 \text{ μeV}}\right)^4, \tag{C4}$$

which can be reached over a timescale of about

$$\tau_{\rm rel} \approx 9 \times 10^{12} \text{ Gyr} \left(\frac{f_a}{10^5 \text{ GeV}}\right)^4 \left(\frac{m}{1 \text{ μeV}}\right)^3 \left(\frac{240 \text{ km/s}}{v}\right)^2, \tag{C5}$$

where $\tau_{\rm rel} \sim \rho_{\rm dm}^{-2}$. If $\lambda > 0$, then the ultimately formed halo should be stable.

[1] R. H. Dicke, The Sun's rotation and relativity, Nature (London) **202**, 432 (1964).
[2] Dicke [1] noted that the existing GR test from the measured excess of Mercury's perihelion precession, of claimed ∼1% precision, neglected the effects of solar oblateness. Its inclusion could thus open the possibility of non-GR contributions.
[3] R. H. Dicke and H. M. Goldenberg, Solar oblateness and general relativity, Phys. Rev. Lett. **18**, 313 (1967).
[4] J. P. Rozelot and C. Damiani, History of solar oblateness measurements and interpretation, Eur. Phys. J. H **36**, 407 (2011).
[5] R. H. Dicke, J. R. Kuhn, and K. G. Libbrecht, The variable oblateness of the Sun: Measurements of 1984, Astrophys. J. **311**, 1025 (1986).
[6] R. H. Dicke, J. R. Kuhn, and K. G. Libbrecht, Is the solar oblateness variable? Measurements of 1985, Astrophys. J. **318**, 451 (1987).
[7] Borexino Collaboration, Experimental evidence of neutrinos produced in the CNO fusion cycle in the Sun, Nature (London) **587**, 577 (2020).
[8] S. Appel *et al.* (Borexino Collaboration), Improved measurement of solar neutrinos from the carbon-nitrogen-oxygen cycle by Borexino and its implications for the standard solar model, Phys. Rev. Lett. **129**, 252701 (2022).
[9] D. Basilico *et al.* (Borexino Collaboration), Final results of Borexino on CNO solar neutrinos, Phys. Rev. D **108**, 102005 (2023).
[10] E. Magg, M. Bergemann, A. Serenelli, M. Bautista, B. Plez, U. Heiter, J. M. Gerber, H.-G. Ludwig, S. Basu, J. W. Ferguson, H. C. Gallego, S. Gamrath, P. Palmeri, and P. Quinet, Observational constraints on the origin of the elements. IV. Standard composition of the Sun, Astron. Astrophys. **661**, A140 (2022).
[11] M. Asplund, A. M. Amarsi, and N. Grevesse, The chemical make-up of the Sun: A 2020 vision, Astron. Astrophys. **653**, A141 (2021).
[12] S. Basu and H. M. Antia, Helioseismology and solar abundances, Phys. Rep. **457**, 217 (2008).
[13] Q.-S. Zhang, Y. Li, and J. Christensen-Dalsgaard, Solar models with convective overshoot, solar-wind mass loss, and PMS disk accretion: Helioseismic quantities, Li depletion, and neutrino fluxes, Astrophys. J. **881**, 103 (2019).
[14] As noted by [15], such would be at odds with the standard assumption of a homogeneous zero-age Sun.
[15] W. C. Haxton and A. M. Serenelli, CN cycle solar neutrinos and the Sun's primordial core metallicity, Astrophys. J. **687**, 678 (2008).
[16] M. Kunitomo and T. Guillot, Imprint of planet formation in the deep interior of the Sun, Astron. Astrophys. **655**, A51 (2021).
[17] M. Kunitomo, T. Guillot, and G. Buldgen, Evidence of a signature of planet formation processes from solar neutrino fluxes, Astron. Astrophys. **667**, L2 (2022).
[18] G. Stenborg, J. R. Stauffer, and R. A. Howard, Evidence for a circumsolar dust ring near Mercury's orbit, Astrophys. J. **868**, 74 (2018).
[19] R. Howard and G. Stenborg (private communications).
[20] P. Pokorný, A. N. Deutsch, and M. J. Kuchner, Mercury's circumsolar dust ring as an imprint of a recent impact, Planetary Sci. J. **4**, 33 (2023).
[21] K. Brecher, A. Brecher, P. Morrison, and I. Wasserman, Is there a ring around the Sun?, Nature (London) **282**, 50 (1979).
[22] J. J. Rawal and S. Ramadurai, Are there rings around the Sun?, Earth Moon Planets **108**, 95 (2012).
[23] L. Iorio, Orbital perturbations due to massive rings, Earth Moon Planets **108**, 189 (2012).
[24] C. M. Will, New general relativistic contribution to Mercury's perihelion advance, Phys. Rev. Lett. **120**, 191101 (2018).
[25] C. W. Misner, K. S. Thorne, and J. A. Wheeler, *Gravitation* (W. H. Freeman, San Francisco, 1973).
[26] R. Mecheri, T. Abdelatif, A. Irbah, J. Provost, and G. Berthomieu, New values of gravitational moments J_2 and J_4 deduced from helioseismology, Sol. Phys. **222**, 191 (2004).
[27] S. Gardner, A. Hinkel, and B. Yanny, Applying Noether's theorem to matter in the Milky Way: Evidence for external perturbations and non-steady-state effects from Gaia Data Release 2, Astrophys. J. **890**, 110 (2020).
[28] A. Hinkel, S. Gardner, and B. Yanny, Probing axial symmetry breaking in the galaxy with Gaia data release 2, Astrophys. J. **893**, 105 (2020).
[29] R. H. Dicke, The solar oblateness and the gravitational quadrupole moment, Astrophys. J. **159**, 1 (1970).
[30] A. E. Roy, *Orbital Motion* (Institute of Physics Publishing, Bristol, United Kingdom, 2005).
[31] R. S. Park, W. M. Folkner, A. S. Konopliv, J. G. Williams, D. E. Smith, and M. T. Zuber, Precession of Mercury's perihelion from ranging to the MESSENGER spacecraft, Astron. J. **153**, 121 (2017).
[32] A. Genova, E. Mazarico, S. Goossens, F. G. Lemoine, G. A. Neumann, D. E. Smith, and M. T. Zuber, Solar System expansion and strong equivalence principle as seen by the NASA MESSENGER mission, Nat. Commun. **9**, 289 (2018).
[33] S. C. Solomon *et al.*, The MESSENGER mission to Mercury: Scientific objectives and implementation, Planet. Space Sci. **49**, 1445 (2001).
[34] C. Ma *et al.*, The second realization of the international celestial reference frame by very long baseline interferometry, IERS Tech. Note **35**, 1 (2009), https://www.iers.org/SharedDocs/Publikationen/EN/IERS/Publications/tn/TechnNote35/tn35.pdf?__blob=publicationFile&v=1.
[35] A. Einstein, Die Grundlage der allgemeinen Relativitätstheorie, Ann. Phys. (Berlin) **354**, 769 (1916).
[36] F. P. Pijpers, Helioseismic determination of the solar gravitational quadrupole moment, Mon. Not. R. Astron. Soc. **297**, L76 (1998).
[37] B. Bertotti, L. Iess, and P. Tortora, A test of general relativity using radio links with the Cassini spacecraft, Nature (London) **425**, 374 (2003).
[38] K. Nordtvedt, Jr., Equivalence principle for massive bodies. II. Theory, Phys. Rev. **169**, 1017 (1968).
[39] C. M. Will and K. Nordtvedt, Jr., Conservation laws and preferred frames in relativistic gravity. I. Preferred-frame

theories and an extended PPN formalism, Astrophys. J. **177**, 757 (1972).
[40] E. V. Pitjeva, N. P. Pitjev, D. A. Pavlov, and C. C. Turygin, Estimates of the change rate of solar mass and gravitational constant based on the dynamics of the Solar System, Astron. Astrophys. **647**, A141 (2021).
[41] A. Fienga and O. Minazzoli, Testing theories of gravity with planetary ephemerides, Living Rev. Relativity **27**, 1 (2024).
[42] C. Leinert, I. Richter, E. Pitz, and B. Planck, The zodiacal light from 1.0 to 0.3 A.U. as observed by the HELIOS space probes, Astron. Astrophys. **103**, 177 (1981), https://articles.adsabs.harvard.edu/pdf/1981A%26A...103..177L.
[43] C. Leinert, M. Hanner, I. Richter, and E. Pitz, The plane of symmetry of interplanetary dust in the inner Solar System., Astron. Astrophys. **82**, 328 (1980), https://articles.adsabs.harvard.edu/pdf/1980A%26A....82..328L.
[44] R. Brasser and S. J. Mojzsis, The partitioning of the inner and outer Solar System by a structured protoplanetary disk, Nat. Astron. **4**, 492 (2020).
[45] M. Sommer, Alpha-meteoroids then and now: Unearthing an overlooked micrometeoroid population, Planet. Space Sci. **236**, 105751 (2023).
[46] A. G. Taylor, J. K. Steckloff, D. Z. Seligman, D. Farnocchia, L. Dones, D. Vokrouhlicky, D. Nesvorny, and M. Micheli, The dynamical origins of the dark comets and a proposed evolutionary track, Icarus **420**, 116207 (2024).
[47] M. L. Kaiser, T. Kucera, J. Davila, O. St Cyr, M. Guhathakurta, and E. Christian, The stereo mission: An introduction, Space Sci. Rev. **136**, 5 (2008).
[48] NASA asteroid fact sheet, https://nssdc.gsfc.nasa.gov/planetary/factsheet/asteroidfact.html.
[49] S. Gardner, S. D. McDermott, and B. Yanny, The Milky Way, coming into focus: Precision astrometry probes its evolution and its dark matter, Prog. Part. Nucl. Phys. **121**, 103904 (2021).
[50] P. Sikivie and S. Wick, Solar wakes of dark matter flows, Phys. Rev. D **66**, 023504 (2002).
[51] M. S. Alenazi and P. Gondolo, Phase-space distribution of unbound dark matter near the Sun, Phys. Rev. D **74**, 083518 (2006).
[52] A. H. G. Peter, Dark matter in the Solar System I: The distribution function of WIMPs at the Earth from solar capture, Phys. Rev. D **79**, 103531 (2009).
[53] I. B. Khriplovich and D. L. Shepelyansky, Capture of dark matter by the Solar System, Int. J. Mod. Phys. D **18**, 1903 (2009).
[54] S. K. Lee, M. Lisanti, A. H. G. Peter, and B. R. Safdi, Effect of gravitational focusing on annual modulation in dark-matter direct-detection experiments, Phys. Rev. Lett. **112**, 011301 (2014).
[55] Y. Sofue, Gravitational focusing of low-velocity dark matter on the Earth's surface, Galaxies **8**, 42 (2020).
[56] H. Kim and A. Lenoci, Gravitational focusing of wave dark matter, Phys. Rev. D **105**, 063032 (2022).
[57] A. H. G. Peter, Dark matter in the Solar System III: The distribution function of WIMPs at the Earth from gravitational capture, Phys. Rev. D **79**, 103533 (2009).
[58] R. K. Leane and J. Smirnov, Floating dark matter in celestial bodies, J. Cosmol. Astropart. Phys. 10 (2023) 057.
[59] R. K. Leane and J. Smirnov, Dark matter capture in celestial objects: Treatment across kinematic and interaction regimes, J. Cosmol. Astropart. Phys. 12 (2023) 040.
[60] B. Dasgupta, A. Gupta, and A. Ray, Dark matter capture in celestial objects: Improved treatment of multiple scattering and updated constraints from white dwarfs, J. Cosmol. Astropart. Phys. 08 (2019) 018.
[61] B. Dasgupta, A. Gupta, and A. Ray, Dark matter capture in celestial objects: Light mediators, self-interactions, and complementarity with direct detection, J. Cosmol. Astropart. Phys. 10 (2020) 023.
[62] J. Bramante, J. Kumar, G. Mohlabeng, N. Raj, and N. Song, Light dark matter accumulating in planets: Nuclear scattering, Phys. Rev. D **108**, 063022 (2023).
[63] A. Ray, Celestial objects as strongly-interacting nonannihilating dark matter detectors, Phys. Rev. D **107**, 083012 (2023).
[64] G. D. Mack, J. F. Beacom, and G. Bertone, Towards closing the window on strongly interacting dark matter: Far-reaching constraints from Earth's heat flow, Phys. Rev. D **76**, 043523 (2007).
[65] S. L. Adler, Placing direct limits on the mass of Earth-bound dark matter, J. Phys. A **41**, 412002 (2008).
[66] S. L. Adler, Planet-bound dark matter and the internal heat of Uranus, Neptune, and hot-Jupiter exoplanets, Phys. Lett. B **671**, 203 (2009).
[67] D. Budker, J. Eby, M. Gorghetto, M. Jiang, and G. Perez, A generic formation mechanism of ultralight dark matter solar halos, J. Cosmol. Astropart. Phys. 12 (2023) 021.
[68] T. Gherghetta and A. Shkerin, Probing a local dark matter halo with neutrino oscillations, Phys. Rev. D **108**, 095009 (2023).
[69] Y. Bai, S. Lu, and N. Orlofsky, Dark exoplanets, Phys. Rev. D **108**, 103026 (2023).
[70] G. Prézeau, Dense dark matter hairs spreading out from Earth, Jupiter, and other compact bodies, Astrophys. J. **814**, 122 (2015).
[71] M. Korwar, Macroscopic dark matter, Ph.D. thesis, University of Wisconsin, Madison, 2023, https://digital.library.wisc.edu/1711.dl/ZIBXFRW6N4UCC85.
[72] Y. Bai, J. Berger, M. Korwar, and N. Orlofsky, Phenomenology of magnetic black holes with electroweak-symmetric coronas, J. High Energy Phys. 10 (2020) 210.
[73] A. M. Green, Primordial black holes as a dark matter candidate—A brief overview, Nucl. Phys. **B1003**, 116494 (2024).
[74] T. X. Tran, S. R. Geller, B. V. Lehmann, and D. I. Kaiser, Close encounters of the primordial kind: A new observable for primordial black holes as dark matter, Phys. Rev. D **110**, 063533 (2024).
[75] A. Ray, R. Laha, J. B. Muñoz, and R. Caputo, Near future MeV telescopes can discover asteroid-mass primordial black hole dark matter, Phys. Rev. D **104**, 023516 (2021).
[76] Y. Du, V. S. H. Lee, Y. Wang, and K. M. Zurek, Macroscopic dark matter detection with gravitational wave experiments, Phys. Rev. D **108**, 122003 (2023).

[77] R. Takahashi, S. Morisaki, and T. Suyama, Probing the solar interior with lensed gravitational waves from known pulsars, Astrophys. J. **957**, 52 (2023).
[78] P. Sikivie, Experimental tests of the "invisible" axion, Phys. Rev. Lett. **51**, 1415 (1983).
[79] J. L. Feng, J. Smolinsky, and P. Tanedo, Detecting dark matter through dark photons from the Sun: Charged particle signatures, Phys. Rev. D **93**, 115036 (2016); **96**, 099903(E) (2017).
[80] J. D. Anderson, E. L. Lau, A. H. Taylor, D. A. Dicus, D. C. Teplitz, and V. L. Teplitz, Bounds on dark matter in solar orbit, Astrophys. J. **342**, 539 (1989).
[81] J. D. Anderson, E. L. Lau, T. P. Krisher, D. A. Dicus, D. C. Rosenbaum, and V. L. Teplitz, Improved bounds on non-luminous matter in solar orbit, Astrophys. J. **448**, 885 (1995).
[82] O. Gron and H. H. Soleng, Experimental limits to the density of dark matter in the Solar System, Astrophys. J. **456**, 445 (1996).
[83] M. Sereno and P. Jetzer, Dark matter vs. modifications of the gravitational inverse-square law. Results from planetary motion in the Solar System, Mon. Not. R. Astron. Soc. **371**, 626 (2006).
[84] I. B. Khriplovich and E. V. Pitjeva, Upper limits on density of dark matter in Solar System, Int. J. Mod. Phys. D **15**, 615 (2006).
[85] J. M. Frère, F.-S. Ling, and G. Vertongen, Bound on the dark matter density in the Solar System from planetary motions, Phys. Rev. D **77**, 083005 (2008).
[86] N. P. Pitjev and E. V. Pitjeva, Constraints on dark matter in the Solar System, Astron. Lett. **39**, 141 (2013).
[87] H. Arakida, Influence of dark matter on light propagation in Solar System, Adv. Space Res. **45**, 1007 (2010).
[88] S. Gardner and D. C. Latimer, Dark matter constraints from a cosmic index of refraction, Phys. Rev. D **82**, 063506 (2010).
[89] J. R. Kuhn, R. I. Bush, M. Emilio, and P. H. Scherrer, On the constancy of the solar diameter. II, Astrophys. J. **613**, 1241 (2004).
[90] M. Emilio, R. I. Bush, J. Kuhn, and P. Scherrer, A changing solar shape, Astrophys. J. Lett. **660**, L161 (2007).
[91] M. D. Fivian, H. S. Hudson, R. P. Lin, and H. J. Zahid, A large excess in apparent solar oblateness due to surface magnetism, Science **322**, 560 (2008).
[92] J. R. Kuhn, R. Bush, M. Emilio, and I. F. Scholl, The precise solar shape and its variability, Science **337**, 1638 (2012).
[93] S. Basu and H. M. Antia, Changes in solar rotation over two solar cycles, Astrophys. J. **883**, 93 (2019).
[94] S. Eren and J.-P. Rozelot, Exploring the temporal variation of the solar quadrupole moment J_2, Astrophys. J. **942**, 90 (2023).
[95] A. S. Konopliv, R. S. Park, and A. I. Ermakov, The Mercury gravity field, orientation, love number, and ephemeris from the MESSENGER radiometric tracking data, Icarus **335**, 113386 (2020).
[96] We note https://hesperia.gsfc.nasa.gov/rhessi3/ for further information and Ref. [92] for discussion of this result and their finding of $\Delta r = 7.20 \pm 0.49$ mas.
[97] A. Auwers, Der Sonnendurchmesser und der Venusdurchmesser nach den Beobachtungen an den Heliometern der deutschen Venus-Expeditionen, Astron. Nachr. **128**, 361 (1891).
[98] This value is employed by Fivian *et al.* [91], though it has been officially updated to 9.5923×10^5 mas by the International Astronomical Union in 2015 [99], with additional space-based measurements from PICARD/SODISM supporting this later result [100]. For our purposes J_2 is sufficiently small that this refinement does not matter.
[99] A. Prša *et al.*, Nominal values for selected solar and planetary quantities: IAU 2015 resolution B3, Astron. J. **152**, 41 (2016).
[100] M. Meftah, T. Corbard, A. Hauchecorne, F. Morand, R. Ikhlef, B. Chauvineau, C. Renaud, A. Sarkissian, and L. Damé, Solar radius determined from PICARD/SODISM observations and extremely weak wavelength dependence in the visible and the near-infrared, Astron. Astrophys. **616**, A64 (2018).
[101] R. Mecheri and M. Meftah, Updated values of solar gravitational moments J_{2n} using HMI helioseismic inference of internal rotation, Mon. Not. R. Astron. Soc. **506**, 2671 (2021).
[102] T. Corbard and M. Thompson, The subsurface radial gradient of solar angular velocity from MDI f-mode observations, Sol. Phys. **205**, 211 (2002).
[103] The error was assessed by accounting for their differences and multiplying by two. A. Genova (private communication).
[104] MDI and HMI rotation data from the global helioseismology pipeline, available online at the JSOC, http://jsoc.stanford.edu/.
[105] T. P. Larson and J. Schou, Improved helioseismic analysis of medium-ℓ data from the Michelson Doppler imager, Sol. Phys. **290**, 3221 (2015).
[106] T. P. Larson and J. Schou, Global-mode analysis of full-disk data from the Michelson Doppler imager and the helioseismic and magnetic imager, Sol. Phys. **293**, 29 (2018).
[107] P. Morel and Y. Lebreton, CESAM: A free code for stellar evolution calculations, Astrophys. Space Sci. **316**, 61 (2008).
[108] J. Christensen-Dalsgaard, ASTEC—The Aarhus STellar evolution code, Astrophys. Space Sci. **316**, 13 (2008).
[109] J. P. Rozelot and S. Eren, Exploring the temporal variation of the solar quadrupole moment from relativistic gravitation contributions: A fortuitous circumstance?, Adv. Space Res. **65**, 2821 (2020).
[110] H. M. Antia, S. M. Chitre, and D. O. Gough, Temporal variations in the Sun's rotational kinetic energy, Astron. Astrophys. **477**, 657 (2008).
[111] I. W. Roxburgh, Gravitational multipole moments of the Sun determined from helioseismic estimates of the internal structure and rotation, Astron. Astrophys. **377**, 688 (2001).
[112] J. Binney and S. Tremaine, *Galactic Dynamics: Second Edition* (Princeton University Press, Princeton, NJ, 2008).

[113] A. Fetter and J. Walecka, *Theoretical Mechanics of Particles and Continua*, Dover Books on Physics (Dover Publications, New York, 2003).
[114] J. D. Anderson, T. V. Johnson, G. Schubert, S. Asmar, R. A. Jacobson, D. Johnston, E. L. Lau, G. Lewis, W. B. Moore, A. Taylor, P. C. Thomas, and G. Weinwurm, Amalthea's density is less than that of water, Science **308**, 1291 (2005).
[115] E. Bois and J. Girard, Impact of the quadrupole moment of the Sun on the dynamics of the Earth-Moon system, Int. Astron. Union Colloq. **172**, 329 (1999).
[116] J. O. Dickey, P. L. Bender, J. E. Faller, X. X. Newhall, R. L. Ricklefs, J. G. Ries, P. J. Shelus, C. Veillet, A. L. Whipple, J. R. Wiant, J. G. Williams, and C. F. Yoder, Lunar laser ranging: A continuing legacy of the Apollo program, Science **265**, 482 (1994).
[117] F. James, *Statistical Methods in Experimental Physics*, 2nd ed. (World Scientific Publishing Company, Singapore, 2006).
[118] G. J. Feldman and R. D. Cousins, A unified approach to the classical statistical analysis of small signals, Phys. Rev. D **57**, 3873 (1998).
[119] G. Stenborg, R. A. Howard, P. Hess, and B. Gallagher, PSP/WISPR observations of dust density depletion near the Sun. I. Remote observations to 8 $R_\odot$ from an observer between 0.13 and 0.35 AU, Astron. Astrophys. **650**, A28 (2021).
[120] P. Tanga *et al.*, Gaia data release 3. The Solar System survey, Astron. Astrophys. **674**, A12 (2023).
[121] M. Tamta, N. Raj, and P. Sharma, Breaking into the window of primordial black hole dark matter with x-ray microlensing, Phys. Rev. D **111**, 043043 (2025).
[122] R. Della Monica and I. de Martino, Bounding the mass of ultralight bosonic dark matter particles with the motion of the S2 star around Sgr A*, Phys. Rev. D **108**, L101303 (2023).
[123] E. V. Pitjeva and N. P. Pitjev, Development of planetary ephemerides EPM and their applications, Celest. Mech. Dyn. Astron. **119**, 237 (2014).
[124] C. A. J. O'Hare, Cosmology of axion dark matter, Proc. Sci. COSMICWISPers (2024) 040 [arXiv:2403.17697].
[125] M. Kobayashi, H. Shibata, K. Nogami, M. Fujii, S. Hasegawa, M. Hirabayashi, T. Hirai, T. Iwai, H. Kimura, T. Miyachi, M. Nakamura, H. Ohashi, S. Sasaki, S. Takechi, H. Yano, H. Krüger, A.-K. Lohse, R. Srama, P. Strub, and E. Grün, Mercury dust monitor (MDM) onboard the Mio orbiter of the BepiColombo mission, Space Sci. Rev. **216**, 144 (2020).
[126] A. Singhal (JUNO Collaboration), JUNO's sensitivity to ^{7}Be, pep and CNO solar neutrinos, Proc. Sci. EPS-HEP2023 (**2024**) 193.
[127] H. von Zeipel, The radiative equilibrium of a rotating system of gaseous masses, Mon. Not. R. Astron. Soc. **84**, 665 (1924).
[128] R. H. Dicke, J. R. Kuhn, and K. G. Libbrecht, Oblateness of the Sun in 1983 and relativity, Nature (London) **316**, 687 (1985).
[129] H. A. Hill and R. T. Stebbins, The intrinsic visual oblateness of the Sun, Astrophys. J. **200**, 471 (1975).
[130] B. J. Beardsley, The visual shape and multipole moments of the Sun, Ph.D. thesis, University of Arizona, 1987, https://repository.arizona.edu/handle/10150/184229.
[131] E. Maier, L. Twigg, and S. Sofia, Preliminary results of a balloon flight of the solar disk sextant, Astrophys. J. **389**, 447 (1992).
[132] A. Egidi, B. Caccin, S. Sofia, W. Heaps, W. Hoegy, and L. Twigg, High-precision measurements of the solar diameter and oblateness by the solar disk sextant (SDS) experiment, Sol. Phys. **235**, 407 (2006).
[133] A. Irbah, M. Meftah, A. Hauchecorne, D. Djafer, T. Corbard, M. Bocquier, and E. M. Cisse, New space value of the solar oblateness obtained with PICARD, Astrophys. J. **785**, 89 (2014).
[134] M. Meftah, A. Irbah, A. Hauchecorne, T. Corbard, S. Turck-Chièze, J. F. Hochedez, P. Boumier, A. Chevalier, S. Dewitte, S. Mekaoui, and D. Salabert, On the determination and constancy of the solar oblateness, Sol. Phys. **290**, 673 (2015).
[135] H. A. Hill and T. P. Caudell, Confirmation of the detection and classification of low-order, low-degree solar acoustic modes with the 1978 solar diameter observations, Astrophys. J. **299**, 517 (1985).
[136] P. H. Scherrer, R. S. Bogart, R. I. Bush, J. T. Hoeksema, A. G. Kosovichev, J. Schou, W. Rosenberg, L. Springer, T. D. Tarbell, A. Title, C. J. Wolfson, and I. Zayer, The solar oscillations investigation—Michelson Doppler imager, in *The SOHO Mission* (Springer, Netherlands, 1995), pp. 129–188.
[137] F. Hill *et al.*, The solar acoustic spectrum and eigenmode parameters, Science **272**, 1292 (1996).
[138] D. Gough, Internal rotation and gravitational quadrupole moment of the Sun, Nature (London) **298**, 334 (1982).
[139] J. Christensen-Dalsgaard, D. O. Gough, and J. G. Morgan, Dirty solar models, Astron. Astrophys. **73**, 121 (1979), https://articles.adsabs.harvard.edu/pdf/1979A%26A....73..121C; **79(E)**, 260 (1979), https://articles.adsabs.harvard.edu/pdf/1979A%26A....79..260C.
[140] J. Duvall, T. L., W. A. Dziembowski, P. R. Goode, D. O. Gough, J. W. Harvey, and J. W. Leibacher, Internal rotation of the Sun, Nature (London) **310**, 22 (1984).
[141] H. A. Hill, G. R. Rabaey, and R. D. Rosenwald, The Sun's gravitational quadrupole moment inferred from the fine structure of the acoustic and gravity normal mode spectra of the Sun, in *Relativity in Celestial Mechanics and Astrometry. High Precision Dynamical Theories and Observational Verifications*, edited by J. Kovalevsky and V. A. Brumberg (Kluwer Academic Publishers, Hingham, MA, 1986), Vol. 114, p. 345.
[142] J. Christensen-Dalsgaard *et al.*, The current state of solar modeling, Science **272**, 1286 (1996).
[143] J. Armstrong and J. R. Kuhn, Interpreting the solar limb shape distortions, Astrophys. J. **525**, 533 (1999).
[144] J. Christensen-Dalsgaard, Solar models with enhanced energy transport in the core, Astrophys. J. **385**, 354 (1992).
[145] S. Godier and J. P. Rozelot, Relationships between the quadrupole moment and the internal layers of the Sun, in *Magnetic Fields and Solar Processes*, ESA Special Publication Vol. 448, edited by A. Wilson *et al.* (1999), pp. 111–115, https://articles.adsabs.harvard.edu/pdf/1999ESASP.448..111G.
[146] S. Godier and J.-P. Rozelot, Quadrupole moment of the Sun. Gravitational and rotational potentials, Astron.

Astrophys. **350**, 310 (1999), https://articles.adsabs.harvard.edu/pdf/1999A%26A...350..310G.

[147] O. Richard, S. Vauclair, C. Charbonnel, and W. A. Dziembowski, New solar models including helioseismological constraints and light-element depletion, Astron. Astrophys. **312**, 1000 (1996), https://articles.adsabs.harvard.edu/pdf/1996A%26A...312.1000R.

[148] K. I. Marchenkov, I. W. Roxburgh, and S. V. Vorontsov, Non linear inversion for the hydrostatic structure of the solar interior, Astrophys. Space Sci. **261**, 51 (1998).

[149] H. M. Antia, S. M. Chitre, and M. J. Thompson, The Sun's acoustic asphericity and magnetic fields in the solar convection zone, Astron. Astrophys. **360**, 335 (2000), https://articles.adsabs.harvard.edu/pdf/2000A%26A...360..335A.

[150] R. van der Zwaard and D. Dirkx, The influence of dynamic solar oblateness on tracking data analysis from past and future Mercury missions, Remote Sens. **14**, 4139 (2022).

[151] A. Fienga, L. Bigot, D. Mary, P. Deram, A. Di Ruscio, L. Bernus, M. Gastineau, and J. Laskar, Evolution of INPOP planetary ephemerides and Bepi-Colombo simulations, IAU Symp. **364**, 31 (2019).

[152] J. H. Lieske and G. W. Null, Icarus and the determination of astronomical constants, Astron. J. **74**, 297 (1969).

[153] I. I. Shapiro, G. H. Pettengill, M. E. Ash, R. P. Ingalls, D. B. Campbell, and R. B. Dyce, Mercury's perihelion advance: Determination by radar, Phys. Rev. Lett. **28**, 1594 (1972).

[154] J. D. Anderson *et al.*, Tests of general relativity using astrometric and radiometric observations of planets, in *27th International Astronautical Federation Congress, Anaheim, CA* (1976).

[155] E. V. Pitjeva, Experimental testing of relativistic effects, variability of the gravitational constant and topography of Mercury surface from radar observations 1964–1989, Celest. Mech. Dyn. Astron. **55**, 313 (1993).

[156] E. V. Pitjeva, Modern numerical ephemerides of planets and the importance of ranging observations for their creation, Celest. Mech. Dyn. Astron. **80**, 249 (2001).

[157] J. G. Williams, D. H. Boggs, J. O. Dickey, and W. M. Folkner, Lunar laser tests of gravitational physics, in *The Ninth Marcel Grossmann Meeting*, edited by V. G. Gurzadyan, R. T. Jantzen, and R. Ruffini (World Scientific Publishing, Singapore, 2002), pp. 1797–1798.

[158] T. I. Afanaseva, M. D. Kislik, Y. F. Kolyuka, and V. F. Tikhonov, Experimental determination of the Sun's flattening, Sov. Astron. **34**, 670 (1990), https://articles.adsabs.harvard.edu/pdf/1990SvA....34..670A.

[159] W. Landgraf, An estimation of the oblateness of Sun from the motion of Icarus, Sol. Phys. **142**, 403 (1992).

[160] J. D. Anderson, E. L. Lau, S. Turyshev, J. G. Williams, and M. M. Nieto, Recent results for Solar-System tests of general relativity, in *Bulletin of the American Astronomical Society* (American Astronomical Society Publishing, 2002), Vol. 34, p. 660.

[161] E. V. Pitjeva, Relativistic effects and solar oblateness from radar observations of planets and spacecraft, Astron. Lett. **31**, 340 (2005).

[162] M. Standish and J. Williams, Orbital ephemerides of the sun, moon, and planets, in *Explanatory Supplement to the Astronomical Almanac*, edited by P. Seidelmann (University Science Books, Melville, NY, 2006).

[163] V. Viswanathan, A. Fienga, M. Gastineau, and J. Laskar, INPOP17a planetary ephemerides, Notes Sci. Tech. l'Inst. Mec. Celeste **108** (2017), 10.13140/RG.2.2.24384.43521.

[164] A. Fienga, J. Laskar, T. Morley, H. Manche, P. Kuchynka, C. Le Poncin-Lafitte, F. Budnik, M. Gastineau, and L. Somenzi, INPOP08, a 4-D planetary ephemeris: From asteroid and time-scale computations to ESA Mars Express and Venus Express contributions, Astron. Astrophys. **507**, 1675 (2009).

[165] A. S. Konopliv, S. W. Asmar, W. M. Folkner, Ö. Karatekin, D. C. Nunes, S. E. Smrekar, C. F. Yoder, and M. T. Zuber, Mars high resolution gravity fields from MRO, Mars seasonal gravity, and other dynamical parameters, Icarus **211**, 401 (2011).

[166] E. V. Pitjeva and N. P. Pitjev, Relativistic effects and dark matter in the Solar System from observations of planets and spacecraft, Mon. Not. R. Astron. Soc. **432**, 3431 (2013).

[167] A. Fienga, J. Laskar, P. Kuchynka, H. Manche, G. Desvignes, M. Gastineau, I. Cognard, and G. Theureau, The INPOP10A planetary ephemeris and its applications in fundamental physics, Celest. Mech. Dyn. Astron. **111**, 363–385 (2011).

[168] A. Fienga, J. Laskar, P. Exertier, H. Manche, and M. Gastineau, Numerical estimation of the sensitivity of INPOP planetary ephemerides to general relativity parameters, Celest. Mech. Dyn. Astron. **123**, 325 (2015).

[169] A. K. Verma, A. Fienga, J. Laskar, H. Manche, and M. Gastineau, Use of messenger radioscience data to improve planetary ephemeris and to test general relativity, Astron. Astrophys. **561**, A115 (2014).

[170] A. Fienga, P. Deram, V. Viswanathan, A. D. Ruscio, L. Bernus, D. Durante, M. Gastineau, and J. Laskar, INPOP19a planetary ephemerides, Research Report, IMCCE, 2019, https://www.imcce.fr/content/medias/recherche/equipes/asd/inpop/inpop19a_20191214.pdf.

[171] A. Fienga, P. Deram, A. Di Ruscio, V. Viswanathan, J. I. B. Camargo, L. Bernus, M. Gastineau, and J. Laskar, INPOP21a planetary ephemerides, Notes Sci. Tech. l'Inst. Mec. Celeste **110** (2021), https://www.imcce.fr/content/medias/publications/publications-recherche/nst/docs/S110.pdf.